MINISTRY OF EDUCATION AND RESEARCH

THE ANNALS OF "DUNAREA DE JOS" UNIVERSITY OF GALATI

Fascicle IX
METALLURGY AND MATERIALS SCIENCE

YEAR XXXVIII (XLIII)
December 2020, no. 4

ISSN 2668-4748; e-ISSN 2668-4756

2020
GALATI UNIVERSITY PRESS

EDITORIAL BOARD

THE ANNALS OF "DUNAREA DE JOS" UNIVERSITY OF GALATI
FASCICLE IX. METALLURGY AND MATERIALS SCIENCE
Nº. 4 - 2020, ISSN 2668-4748; e-ISSN 2668-4756
Volume DOI: https://doi.org/10.35219/mms.2020.4

Table of Contents

THE ANNALS OF "DUNAREA DE JOS" UNIVERSITY OF GALATI
FASCICLE IX. METALLURGY AND MATERIALS SCIENCE
Nº. 4 - 2020, ISSN 2668-4748; e-ISSN 2668-4756
Volume DOI: https://doi.org/10.35219/mms.2020.4

THE ANNALS OF "DUNAREA DE JOS" UNIVERSITY OF GALATI
FASCICLE IX. METALLURGY AND MATERIALS SCIENCE
Nº. 4 - 2020, ISSN 2668-4748; e-ISSN 2668-4756
Article DOI: https://doi.org/10.35219/mms.2020.4.01

EXPERIMENTAL SYSTEM FOR CHARGING AND TESTING BATTERIES SPECIFIC TO MULTIROTOR DRONES

Vasile PLESCA, Sanda Victorinne PAȚURCĂ
Politehnica University of Bucharest, Romania
e-mail: adi_plesca@yahoo.com

ABSTRACT

The experimental stand created is made for charging, testing and monitoring the processes that take place at a drone, in a static and also dynamic manner. On this platform we have developed, created and tested various kinds of sensors, and charging methods, rechargeable batteries, multicopper drones, automatically without disconnecting or disassembling them from the drones they serve. Also, at this level we fitted a flat zone, that is polarized where the drone will land, in a controlled manner and after a preliminary testing of polarity and of tension level, the charging will begin, as its parameters will carefully monitored.

KEYWORDS: experimental stand, Li-Po battery, drones, increasing autonomy

1. Introduction

The drone as defined is a UAV device (Unmanned Aerial Vehicle) capable of flying, without being piloted by a person on board, it is automatic and is driven from a distance by a specialised operator, through a remote control. As was the case with the evolution of internet and then of mobile phones, drones have gone being exclusive for military purposes to the civil, where thanks to its remarkable advantages it quickly had a major impact on the industry. At first, due to large costs of owning but mostly maintaining one, they were small and had limited features. But since their limited applications did not raise any interest, and their autonomy was limited by costs, to a usage of only a few minutes, enough for scanning areas that were only visible to the operator, the production costs as well as costs for buying one are fair. As time passed, technological development had led to an increased efficiency and minimising of some hardware components, from the drone's structure, and protocols and specific sensors have evolved, becoming more and more reliable. It was obvious that with this development that their price also continued to drop, so civil drones became more and more like professional drones ensuring a transport capacity sufficient for more and more complex operations. Moreover, the development of phones and tablets has increased the capacity of monitoring and control of such systems, through a remote control and an app that runs on tablets or smartphones and which does not use too many resources.

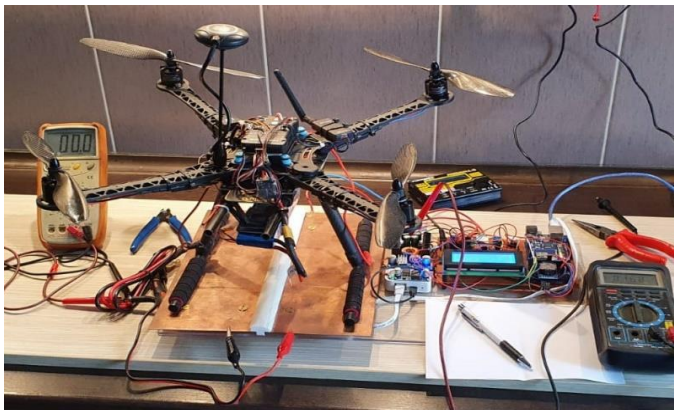

Fig. 1. *Image of the stand for testing and charging drones during calibration*

THE ANNALS OF "DUNAREA DE JOS" UNIVERSITY OF GALATI
FASCICLE IX. METALLURGY AND MATERIALS SCIENCE
Nº. 4 - 2020, ISSN 2668-4748; e-ISSN 2668-4756
Article DOI: https://doi.org/10.35219/mms.2020.4.01

With this in mind, technological limitations still exist, mostly concerning charging, because of the weak development of batteries. Finding an optimal battery is a constant concern of all factors present here. The goal is finding a balance between performance, flight time and battery charging capacity. Li-Ion and Li-Polymer batteries are most commonly used ones because of their large energy capacity and discharge capacity. In static mode this battery is well known and its charging and discharging capacities are relatively well known if a known charger is used for the specific voltage and power of that battery. The problems occur when the charging is automatic, autonomous, because in the case of an error the result will be a large flame or an explosion. There have been various attempts to make drone charging automatic, but none have as far as to completely automatise the whole process of charging, for this kind of batteries to become autonomous, this is what we all want. So, drones are captive to an operator that has to monitor the charging process, even if the drones have to be ordered from thousands of km away.

2. Automatic system for charging drone batteries

The presence of drones in industry has brought a lot of changes in many fields, mostly taking away the burden that existed before they were invented. Increasing the flight autonomy and automating the charging process would allow the drones to work autonomously, according to algorithms clearly implemented at their level, or be controlled from remote locations, without needing the presence of a human operator in the monitored location.

From the energy analysis performed on several types of drones, the biggest consumer of a drone is the propulsion system, for example the engines that can be a minimum of 3 or maximum 8, with continuous operation, at speeds and variable energy consumption depending on the piloting style and the mission at hand. Another important consumer is the telemetry system, which transmits critical data on board the drone, such as: battery status, geographical position on X, Y and Z and videos, photos, specific to navigation, captured in real time by the video system located on the drone, etc., but which has a predictable consumption, within acceptable limits. Also, on the drone platform is the sensor system that can contain a series of mission-specific sensors and optionally a professional media capture system, in various spectra, visible and/or infrared, depending on the mission profile can be captured, with a consumption that can be estimated. Most of the time this system is placed on a gimbal support, which can be operated remotely. This is another energy consuming element, because it can be driven by 2 or 4 motors, and its consumption cannot be determined [1-3].

All these components have an impact on flight autonomy, being powered by one or two large capacity batteries, which can generally ensure a continuous flight with an average of 30 minutes. But in the case of a repetitive mission that may require flying over a high security zone or an objective with a large enough surface, such as photovoltaic power plants, even if the information captured from the sensors can be easily transmitted remotely, the limitations imposed by the batteries make the presence of specialized personnel at the location mandatory, in order to change the battery packs when they discharge.

Thus, in this paper I will present an automatic system for recharging a multi engine drone's batteries, without disconnecting them from the drone. To do this, I have created an experimental stand where I tested various conductive methods, that had as an object the charging of batteries in completely safe conditions with the possibility of controlling the whole system from distance.

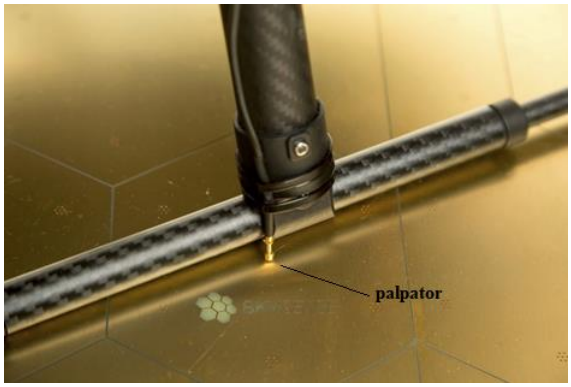

Fig. 2. *Showing the contact system between the padding of the drone and the probe* [3]

This being an experimental stand I have imposed certain limits of weight and electric parameters, thus it had all been thought after for drones with a maximum span of the landing gear of 600 x 250 mm with Li-Ion and Li-Po batteries with a maximum of 6 cells in series, that is about 6S - 22,2 V, 22000 mAh (Figure 1). The whole system is split into 2 main modules; the fixed base, which houses the main charging source, the system controller, the web server for monitoring/ local control or distant control and the only module placed on the drone that contains an BMS – Battery Management System [1, 4, 10] specially built for this autonomous charging source (Figure 3). Between the 2 modules there two clear links, a physical link that which is based on direct power contact between the BMS system placed on the

THE ANNALS OF "DUNAREA DE JOS" UNIVERSITY OF GALATI
FASCICLE IX. METALLURGY AND MATERIALS SCIENCE
Nº. 4 - 2020, ISSN 2668-4748; e-ISSN 2668-4756
Article DOI: https://doi.org/10.35219/mms.2020.4.01

drone and the charging area through some probes installed on the landing gear of the drone and a wireless link through which data collected from the BMS system are integrated in the implemented algorithm of the microprocessor placed on the fixed padding. The contact areas of the stand are made of a board with copper probes to ensure a perfect contact between the poles of the system; starting the charging process is done only once the drone has landed and firmly contacts the ground without generating disturbances because of the electric arc.

All monitoring and safety systems have been doubled according to recommendations of the IEEE 1625-2008 standard [4], practically eliminating the errors or problems caused by a fault at the sensors.

The components of the system are simple but work in tandem according to a well-developed algorithm that responds efficiently to the events that occur. According to the place where they are placed in the system, they are mostly mounted on the stand, only a small part is placed on the drone.

The ones located on the drone actually deal with the protection of the battery and the drone they serve. All the modules located here are miniature and chosen especially by the lowest possible weight, because through the system described here, I do not want to decrease its main characteristics: transport capacity and manoeuvrability of the drone. At the drone level, the most important parameter monitored by BMS is the battery temperature; the temperature reading is done with the DS1820 digital sensor, which has a measuring range between -55 °C ÷ +125 °C, enough to monitor lithium technology batteries and a resolution of up to 12 bits.

All parameters read at the drone are transmitted to the microcontroller on the base, via a LORA module (Figure 3), which together with the information collected from its sensors makes quick decisions to protect the battery and the drone by default, stopping charging or limiting the charging current, when the situation demands it.

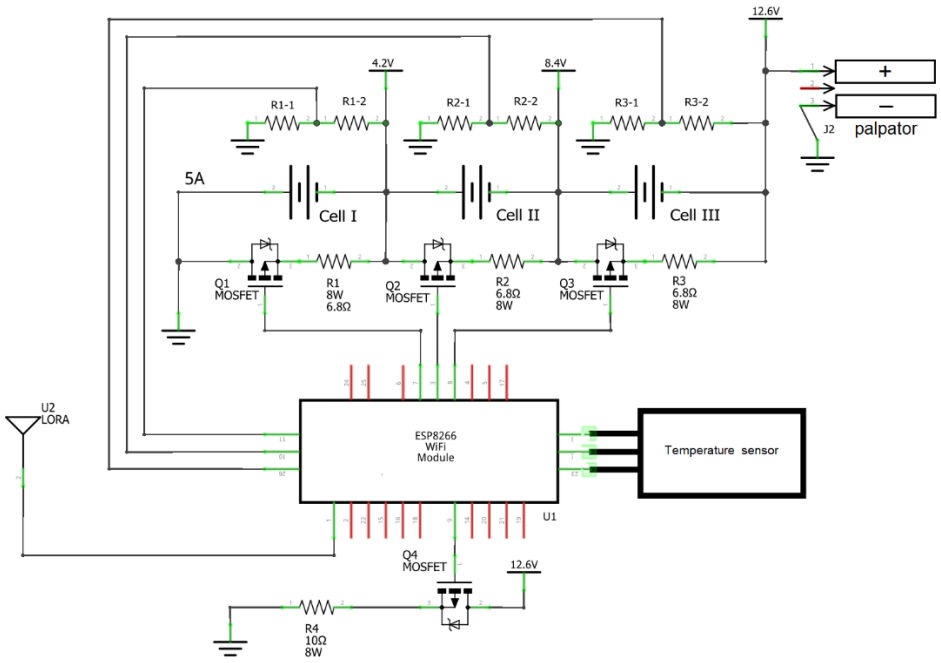

Fig. 3. *General scheme BMS - module located on the drone*

The Li-Po cells that make up these batteries are mini electrochemical systems. Depending on the requirements of the application they serve, to achieve the optimal voltage or capacity, they are interconnected in series or in parallel and are denoted by xSyP, where x is the number of cells in series, and y represents the number of cells in parallel [1, 4, 10]. But each cell has a unique self-discharge rate, a nominal capacity and especially a unique impedance, which varies over time, randomly, depending on several parameters. If the cells are connected in parallel these differences are not a problem during operation, because they will always find a way to balance their voltage level naturally. However, care must be taken that these voltage differences are not large enough to generate current shocks at connection, or rapid temperature rises, which would inevitably lead to the destruction of the cell package. Problems occur when cells are interconnected in series, because the cells are not ideal voltage sources, and the variations are quite large from cell to cell.

THE ANNALS OF "DUNAREA DE JOS" UNIVERSITY OF GALATI
FASCICLE IX. METALLURGY AND MATERIALS SCIENCE
No. 4 - 2020, ISSN 2668-4748; e-ISSN 2668-4756
Article DOI: https://doi.org/10.35219/mms.2020.4.01

The capacity of the battery [mAh] expresses the possible current generated by it in one hour, or half of this current for two hours, etc. until the battery reaches the minimum discharge threshold. Increasing the battery capacity can be done by connecting several cells in parallel [1].

Another quite important element is the "C rate" - the constant discharge of the battery together with the previous parameter provides information about the maximum amperage that can be safely discharged from the battery in a constant way, but also the recommended charging current.

Regarding the voltage at the battery terminals [V], for a LiPo battery, in general, three reference voltages are defined: the nominal voltage specified by the manufacturer, which is generally a multiple of 3.7 x no. of inserted cells, the maximum voltage per cell 4.2 V - the battery is fully charged when each cell reaches this value and the minimum discharge voltage 3.0 V per cell. Theoretically, the maximum voltage at the battery terminals divided by the total number of cells interconnected in series should not exceed 4.2 V per cell. But in practice, during the charging process, things are not like that, and when the voltage in the cells exceeds 4.2 V even by a few hundred millivolts, the cell temperature rises rapidly, destroying the battery [1].

Protecting the battery by stopping the charging process when a cell reaches the maximum level of charging accepted (4.2 V) is not a solution because the charging would not be complete, and an incomplete charging will ruin the battery yield, which is based on a lower usage time given the minimum safety tension (3.0 V) of a cell at a given time and the maximum tension of a cell in the pack (4.2 V). From here comes the need of the maximum possible energy.

Currently, there are two major equilibrium classes: active and passive, that use various circuit topologies. The most used ones have a series of control algorithms, SoC based on history and tension, but both have the same objective: to monitor and balance the charge at each cell. That being said, developing a balance with more characteristics of control implemented would raise the yield and would prolong the life of a battery, but the cost of such a charger would be quite big. So, the producers of such chargers impose a passive equilibrium system.

Types of balancing systems used for Li-Po battery [1, 4, 10]

Cell voltage balancing through By-pass. This type of balancing module uses a simple voltage comparator that controls a power MOSFET mounted in parallel on each cell.

Cell voltage balancing by charge redistribution. Basically, the system tests each cell and through switching circuits transfers the excess energy to the weaker cells. This module is very expensive but it is very efficient and has the great advantage that it does not depend on the current generated by the charger, being able to perform cell balancing in any conditions.

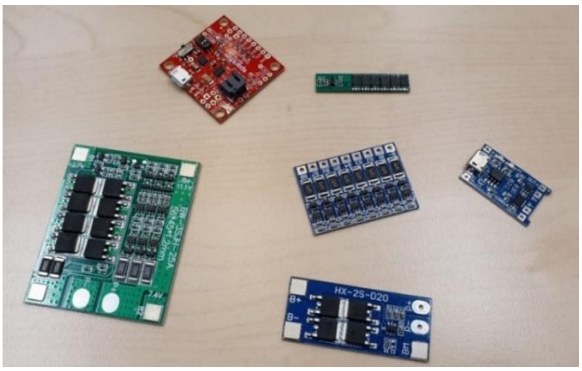

Fig. 4. *Various types of levelling Li-Po cells*

Energy transport between cells. This method also transfers energy to weaker cells but uses capacitors for this so the system is more affordable. Unlike the previous method, this one is very slow and has a fairly large size.

Inductive converter. This balancing system uses the concept of power converter in switching mode and performs balancing directly on each cell, independently of the others. But it has the disadvantage that it is very expensive and has a fairly large size and weight.

Analysing all these balancing methods and taking into account the limitations given by the weight of the BMS to be placed on the drone, and in solidarity with its battery, I have come to the conclusion that creating a minimally customized system is the only solution. In addition, the idea of integrating in the system a standard BMS module like the ones in the previous figure, after testing them I came to the conclusion that none of them offer the necessary specifications, and neither the required safety.

3. Description of the implemented algorithm

The algorithm implemented in this project requires the charging of Li-Polymer batteries using the most common charging method, which follows the alignment of the charging curve in Figure 5. This method has three main phases: preload, constant current charging and constant voltage charging [1, 4, 10].

Phase I. In the preload phase, first of all, the temperature of the environment and of the package of cells that form the battery are tested. If the

THE ANNALS OF "DUNAREA DE JOS" UNIVERSITY OF GALATI
FASCICLE IX. METALLURGY AND MATERIALS SCIENCE
Nº. 4 - 2020, ISSN 2668-4748; e-ISSN 2668-4756
Article DOI: https://doi.org/10.35219/mms.2020.4.01

temperature is not in the optimal temperature range: 0 ÷ 50º Celsius, the beginning of the charging process at low temperatures favours the appearance of metallic lithium which means the accentuated degradation of the electrodes that form the cell, and in case of a temperature above the upper limit results in accelerated degradation of the cell and implicitly of the battery. If the temperature of the cells is within the accepted limits then the charging process begins, charging the battery at a rate of 10% of the nominal charging capacity, up to a voltage of 3.0 V on each cell.

Basically, in this phase the integrity of the cells is tested, thus the passive layer is regenerated, which would be affected if the battery had been stored for a longer period of time, and if the cell voltage does not reach the value of 3.0 V in a predetermined time (30 minutes), then the loading process ends with an error, because structurally or chemically the cells are compromised. If the voltage on each cell exceeds the 3.0 V threshold then the charging process enters phase 2.

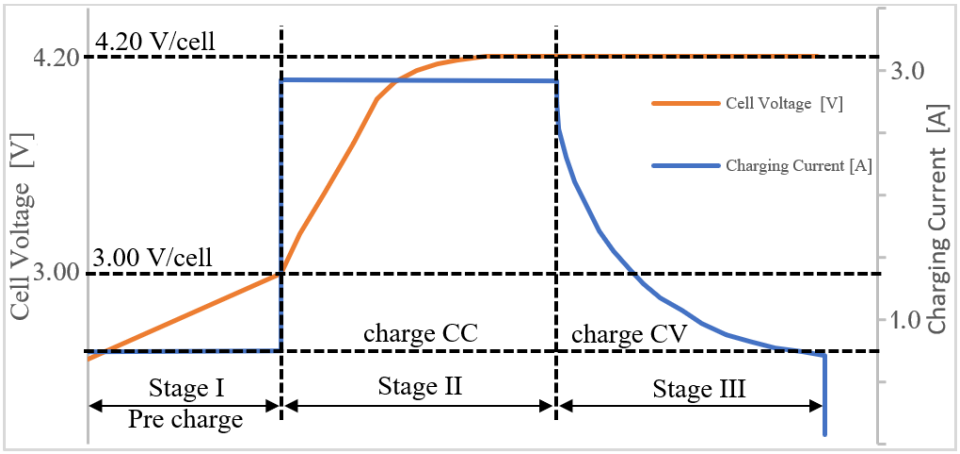

Fig. 5. *LiPo battery charge profile, using the constant current / constant voltage model*

Phase II. In this phase the level of the charging current is kept at a constant, limited from 0.5 C to 1 C, to avoid heating the battery and ruining the cells. For these tests I have kept the charging rate to 1 C, the temperature remaining within the acceptable limits for the test charger. The charging process remains set on these parameters till the tension on each cell reaches the maximum noted on the battery: 4.2 V. Even at this phase the temperature is monitored. If the temperature passes the maximum threshold the charging process is suspended till temperature drops below 45 degrees. When the tension reaches the noted value, we enter phase III.

Phase III. In this phase of the charging process the current begins to drop to a prescribed value and the tension is the to a reference maximum value set in phase II. Lowering the current is done naturally because of the internal resistance of the battery to a value of between 5-10% from the charging current specified on the battery.

As a percentage phase II is about 70% of the total charging time, and phase III is the remaining 30%. Generally speaking, the lower the internal resistance of the battery, the lower the charging time is also, and setting a charging current that is greater makes passing through the two phases quicker. But increasing current for charging over the specified limit makes the lifetime of the battery drop a lot because metallic Lithium appears which sets on the anode. This is an aggressive metal that easily reacts to the electrolyte leading to lithium loss, which in turn leads to a reduction of battery life.

The implemented system here notes when the battery has charged to 100%, by monitoring the charging current, that ultimately drops slowly till it reaches the value of C/20.This value is associated with finishing the charging process, but for safety reasons it can be doubled by measuring tension on each cell of the battery. If all cells have a tension of 4.2 V, then the charging process is done.

Furthermore, as I stated above, during the entire charging process, the battery temperature is continuously monitored, and if it goes over the safety interval the charging process is suspended by the microcontroller. If the charging time is not a critical one then, in order to eliminate the effects that could appear on the battery structure, it is possible to set the charging process to be a slower one, but not longer than 3 to 5 hours, depending on the parameters of the battery, but especially the age and condition of the battery.

Another function implemented in the developed charging stand algorithm is to detect the discharge rate of Li-Po batteries. This is a rather important

THE ANNALS OF "DUNAREA DE JOS" UNIVERSITY OF GALATI
FASCICLE IX. METALLURGY AND MATERIALS SCIENCE
Nº. 4 - 2020, ISSN 2668-4748; e-ISSN 2668-4756
Article DOI: https://doi.org/10.35219/mms.2020.4.01

initial parameter, being imposed by their manufacturer depending on the application it serves, and can vary quite a lot. For this they use thicker or thinner active materials depending on the desired application, the thin layers have a higher loading rate but the energy density is lower. But the discharge rate decreases a lot when the temperature drops below 0 C, but also with the accumulation of a significant number of charging cycles.

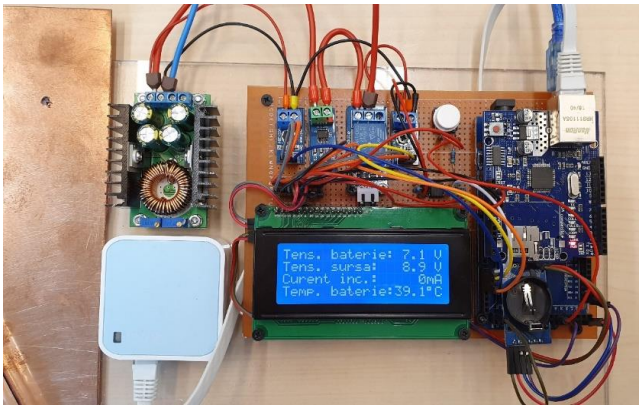

Fig. 6. *The monitoring and command module at the base level*

The necessary function for preparing these batteries for safe storage has also been implemented, for longer periods when the drone is no longer used. Storing Li-Ion batteries for a longer period of time is done by bringing the voltage of each cell to a safety value of 3.7 V, otherwise high voltages will lead to corrosion of electrolytes, which destroy the battery over time. This value of 3.7 V per cell is a minimum accepted because a voltage lower than this can lead to the dissolution of protective layer and also to its irreparable damage. This type of battery, unlike NiCd and NiMH batteries, has an almost imperceptible self-discharge process, so it does not require additional charging/discharging cycles during storage. But storing these batteries at high temperatures can lead to accidents or fires, and storing them at low temperatures increases the shelf life.

4. Security elements implemented in the algorithm

During the charging process but especially during the operating process Li-Polymer batteries can be easily subjected to stress, so the protections that can act externally on the charging process are: overvoltage, overcharging, overcurrent, overtemperature, short to terminal or at the cell.

Overvoltage applied to the terminals of a battery - may occur during the charging process if the main source of the charger has failed. This has the immediate effect of overheating the cells in a very short time, and the result is damage to the cells and in some cases their explosion with fire. To eliminate this event during the charging process, the voltage on each cell and at the base level, on the contact areas, is measured. If the voltage exceeds the imposed limits, the microcontroller commands to stop the charging process, with event recording in the database and will block the process until this defect is reset by a human operator. The same can happen in case of accidental polarity inversion. Thus, when the drone lands on the loading pad, the correctness of the polarity is tested and if the drone has settled properly and the contact is firm, the loading process is started with the observance of all the imposed limits. If the drone did not respect the position drawn for landing then a signal is issued to the drone system and / or to the operator in charge of it, to resume the correct landing process. To determine the polarity at the charging pad, the circuit in the Figure 7 was used, which in case of incorrect polarity will generate a voltage of 5 V at the input of the microcontroller, in which case it will not allow the charging process to begin.

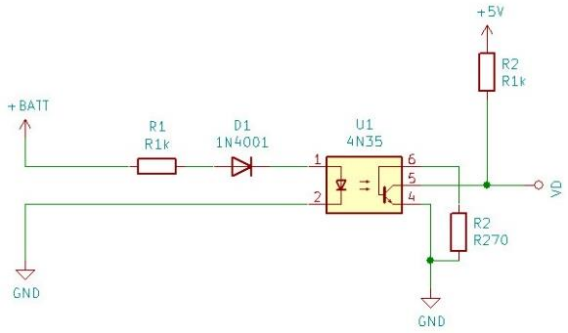

Fig. 7. *Polarity circuit test*

The charging current and the correct polarity are measured during the whole charging process, and in case the drone is disconnected from the source or the

THE ANNALS OF "DUNAREA DE JOS" UNIVERSITY OF GALATI
FASCICLE IX. METALLURGY AND MATERIALS SCIENCE
Nº. 4 - 2020, ISSN 2668-4748; e-ISSN 2668-4756
Article DOI: https://doi.org/10.35219/mms.2020.4.01

polarity of the current changes, the whole process of testing and charging starts from the beginning.

Battery overcharge - This parameter can be determined thanks to the communication modules of LORA type that have a coverage of kilometres. Thus, during flight, the module placed on the drone will send to base information about tension on each cell and temperature of the battery. By analysing the character of the curve of discharging the operator can identify if the choice of drone battery was done correctly or it has structural problems. Generally, a super discharge has an immediate effect over the battery and reduces its life more than it writes it does because at low voltages the copper current collectors of the battery are dissolved. If measures to remedy this are taken quick turning back to normal parameters is done during the charging process when the copper sets on the respective electrodes.

Overcurrent during discharge - the occurrence of overcurrent during discharge of the drone battery on mission may be due to a defect caused by a consumer or even a failure of a cell in the battery component. In general, the battery can withstand an occasional overcurrent but only for a very short time, 10 seconds and within acceptable limits, which in most batteries is twice the rated capacity. When such an event occurs, the battery temperature begins to rise rapidly, so the operator will be warned to make an emergency landing or if the drone flies autonomously it will return to the charging pad, where it will pass into a state of waiting evaluation from a human operator. If the drone does not land in a short time, the battery will overheat, and when its temperature exceeds a critical value of 600 ºC there is a chance of almost 100% that the battery will be destroyed in most cases and it will catch fire.

Overcurrent during charging - during the charging process the current is monitored using a specialized current transducer, so if an overcurrent occurs, the entire system goes into safe mode. In general, the charging current is in the range of 0.7-1 C for ordinary batteries but can obviously be much higher for high power batteries, specially designed for such mode. Obviously, if no action is taken quickly, the immediate effect is to increase the temperature and in the second phase to cover the anode with a Lithium metal powder. This phenomenon electrically disconnects the respective area, and the battery becomes more and more inefficient. If the process continues, the Lithium metal powder reacts with the electrolyte and the temperature in the cell reaches several thousand degrees, resulting in the destruction of the battery. This phenomenon can also occur when charging the batteries at temperatures below zero degrees Celsius, so to avoid it the stand was fitted with a heating element that brings the battery to an acceptable temperature level in compliance with JEITA specifications.

Overvoltage at cell level - supplying the battery with the voltage specified by the manufacturer during the charging process does not eliminate the occurrence of overvoltage in the cells that make it up. This can occur if the cells initially have a different SOC loading level and obviously if the cells have a different self-discharge rate. Within the stand this situation was avoided by the BMS created, monitoring each cell and by means of the microcontroller and the MOSFET, decisions are made to isolate the cell or to reduce the charging current applied to the respective cell, putting in parallel with the resistance power.

Short circuit at the cell or battery level - this type of fault occurs at the cell level and is the most common, but unfortunately conventional chargers do not provide protection at the cell level for this parameter. At the moment, even manufacturers that comply with international standards, specific to these types of batteries, have not developed cell-level protections, focusing on the protection of the entire cell package. The charging system presented here offers this protection on each cell, by isolating them in case of a defect.

In the end we have reached a stable version that includes several types of sensors. The stand tests the electrical parameters of the drone, compares the voltage level and the charging current initially set and if everything is in order, the charging process starts. The whole process is recorded in a database, and all the data can be viewed in an almost instantaneous time in a web page, from where various settings and commands can be executed to the execution elements of the system.

5. Conclusions

Automating the battery charging process, without disconnecting them from the drone, opens new horizons for an autonomous usage regime of drone systems. Thus, these applications that involve the repetitive scanning of some objectives or elements found in areas that are hard to access, can be done autonomously by implementing superior algorithms at the drone and the navigation system. Such applications can be: Perimeters that need continuous security, scanning and defect detection at the level of photovoltaic panels, agricultural crops, etc.

Creating a personalized BMS with complex functions and managed through complex algorithms that run on a microprocessor, increase the duration of functioning of a battery, but mostly accidents that can occur because of fire or explosion of such a battery can be avoided; they mostly lead to the collapse of the whole system of sensors including the drone

support. Besides the fact that such a drone equipped with sensors has a very large cost, where losses can be in the order of thousands of euros, the uncontrolled collapse can generate human and material accidents where it crashes.

During the tests carried out on this stand, a series of characteristics of consumption have been determined at the level of the entire drone. Also, several battery configurations have been tested: 1S1P, 2S1P, 3S1P, 3S2P, etc.

Because of the limited weight but mostly because of the electrical parameters: tension and maximum charging current, that can be set at a given moment, the possibility of testing is extremely limited. In a future test this will be tested and created for electrical solar panels, with a centralized configuration of inverters. Thus, for field tests the generous sizes of the flat roof of these inverters will be used for placing the charging stand.

6. Acknowledgements

The work has been funded by the Operational Program Human Capital of the Ministry of Europe Funds through the Financial Agreement 51675/09.07.2019, SMIS code 125125.

References

[1]. Yevgen Barsukov, Jinrong Qian, *Battery Power Management for Portable Devices*, ISBN 13: 978-1-60807-491-4 ARTECH HOUSE 685 Canton Street Norwood, MA 02062, 2013.
[2]. Kimon P. Valavanis, John Evans, Daniel Felix, George J. Vachtsevanos, *Handbook of Unmanned Aerial Vehicles*, ISBN: 978-90-481-9706-4, 978-90-481-9707-1, Springer Science, Business Media Dordrecht, 2015.
[3]. Clough B., *Metrics, schematics! How do you track a UAV's autonomy?*, In Proceedings of the AIAA 1st Technical Conference and Workshop on Unmanned Aerospace Vehicles, Portsmouth, 2002.
[4]. ***, 1625-2008 - IEEE Standard for Rechargeable Batteries for Multi-Cell Mobile Computing Devices – IEEE 1625-2008, https://ieeexplore.ieee.org/stamp/stamp.jsp?tp=&arnumber=4657368 - 2020.
[5]. ***, https://www.flir.com/products/vue-pro-r/ - 2020.
[6]. ***, https://dronemag.ro/magazin/camere-video-sport/camera-de-termoviziune-flir-vue-pro-640/ - 2020.
[7]. ***, https://www.dronebase.it/prodotto/dual-sensor-ir-eo-gimbal-gemini-ir-2/ - 2020.
[8]. ***, http://www.dummies.com/consumer-electronics/drones/battery-considerations-for-your-drone/ - 2020.
[9]. ***, http://www.dummies.com/consumer-electronics/drones/battery-considerations-for-your-drone/ - 2019.
[10]. ***, http://www.cnydrones.org/LIPO-batteries-and-safety-for-beginners/ - 2019.
[11]. ***, http://www.droneomega.com/quadcopter_battery_guide - 2020.
[12]. ***, http://www.miniquadtestbench.com/ - 2020.
[13]. ***, http://www.dronethusiast.com - 2020.

THE ANNALS OF "DUNAREA DE JOS" UNIVERSITY OF GALATI
FASCICLE IX. METALLURGY AND MATERIALS SCIENCE
Nº. 4 - 2020, ISSN 2668-4748; e-ISSN 2668-4756
Article DOI: https://doi.org/10.35219/mms.2020.4.02

A MOLECULAR DYNAMICS CALCULATION TO CASCADE DAMAGE PROCESSES

Hiwa Mohammad QADR
College of Science, University of Raparin, Sulaimanyah, Iraq
e-mail: hiwa.physics@uor.edu.krd

ABSTRACT

In this work, Molecular dynamics simulation was performed to study the cascade damage evaluation initial from a 250 eV Primary Knock-on Atoms (PKAs) in gold. For this purpose, the simulations were carried out using the molecular dynamics code GRAPE to study the cooling phase of a cascade from the thermodynamic point view. Interatomic interaction of the cascade was investigated by the Morse potential and it is found that during the cooling phase of the cascade local equilibrium was realized.

KEYWORDS: displacement cascade, primary damage, Morse potential, molecular dynamics

1. Introduction

Radiation damage processes from initial defect production to microstructure evolution occur over a wide spectrum of the time and size scale. Atomic collision sequences during the collisional phase continue for a few tenth of picosecond in a small region on nanometer scale. The subsequent cooling phase takes place for nearly 10^{-11} sec [1, 2].

Molecular dynamics method is a well- defined microscopic description of many-body system [3]. Computing the phase space trajectories of a collection of molecules that individually obey classical laws of motion [4], molecular dynamics computer simulations provide the most realistic description of the primary damage state including the collisional and cooling phase. Binary collision approximation provides a realistic description of the gross features of defect spatial distribution with requisite physical reality in statistically significant numbers, including the size, number and spacing of subcascades [5, 6].

The cascade damage methods are classified into four stages (Thermal phase, collisional phase, diffusional phase and cooling phase). The cooling phase is defined as stage of the dissipation of energies deposited locally during the collisional phase, ending when the cascade region reaches thermal equilibrium with its surroundings. During the cooling phase, average kinetic energy in a cascade core is well above the melting temperature of materials and the significant rearrangement of defects takes place, including recombination and clustering, after the cooling phase, interaction of point defects occurs by normal, thermally activated diffusion [7].

Displacement cascade, in a material, can be visualized as a series of elastic collisions initiated with the lattice atoms, where the lattice atom is hit by a high energy particle. The initially-bombard a target is named PKA. The Norgett-Robinson-Torrens (NRT) model suggested that the number of Frenkel pairs produced by a PKA of energy [8-10]. It is used to calculate radiation damage calculation method exposure unit known as displacement per atom (dpa). Thus, dpa has been used as a standard measure for computing proton- neutron induced radiation damage production from different radiation sources [11-15]. Molecular dynamics simulation of processes in metals have been studied by many research groups including temperature dependence of the processes of cascade damage [16-18].

MDGRAPE code is a series of special-purpose computer system built for particle-based simulations such as molecular dynamics simulation [19, 20]. In this paper, the primary states of cascade damage processes are simulated to study the cooling phase in gold, using the molecular dynamics simulation method.

2. Molecular dynamics simulation methods

A major computer simulation method to analyse development processes of cascade damage is GRAPE code to study the cooling phase of a cascade from the

THE ANNALS OF "DUNAREA DE JOS" UNIVERSITY OF GALATI
FASCICLE IX. METALLURGY AND MATERIALS SCIENCE
Nº. 4 - 2020, ISSN 2668-4748; e-ISSN 2668-4756
Article DOI: https://doi.org/10.35219/mms.2020.4.02

thermodynamic point view. Molecular dynamics are performed to study a computational cell and to apply many body interatomic potential based on embedded atom method (EAM) [21] to description of atom behaviour. In this paper, 250 eV cascade is simulated in gold. One atom is chosen as 250 eV PKA in the direction of [120], from the computational cell. Computational cell contains 10800 gold atoms corresponding to a rectangular parallelepiped of $15\alpha_0$ x $15\alpha_0$ x $12\alpha_0$, where α_0 is the lattice constant. For atoms in the vicinity of the boundary of the cell, periodic boundary conditions are employed. A time step equals to 3 x 10^{-15} s for all the calculations. Since the system is thermally insulated, in the present study, interatomic interaction is described using pair- wise Morse potential [22] which is adjusted by the cohesive energy, elastic constants and compressibility of gold.

3. Results and discussion

In this study, Molecular dynamics measurement was performed to study the cooling phase of a cascade in gold, considering from the thermodynamic point view that the initial lattice temperature is 0 K. Figure 1 shows the time dependence of the number of displaced atoms for 250 eV cascade by using Morse potential where a displaced atom is defined to be displaced by over one-quarter of the lattice constant from nearest lattice site. It is also shown that an initial increase is followed by a decrease due to the spontaneous recombination of unstable defect pairs. Furthermore, durations of relaxation phases and collisional are estimated to be both 0.13 psec. It also observes the migration of a small number of interstitial atoms during the following cooling phase.

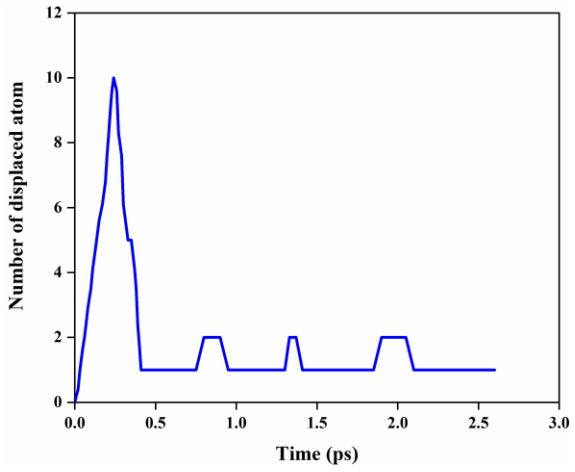

Fig. 1. *Number of displaced atoms as a function of time for a 250 eV cascade in gold using the Morse potential*

Figure 2 shows the time dependence of average kinetic energy. In the collisional phase the average kinetic energy rapidly decreases due to conversion of the kinetic energy to potential energy, establishing approximate equipartition of energy during the subsequent cooling phase, the kinetic energy remains constant due to the thermally insulated system. Furthermore, during the cooling phase, the migration of interstitial atoms with relatively high kinetic energies (0.1 ~ 1 eV) is observed.

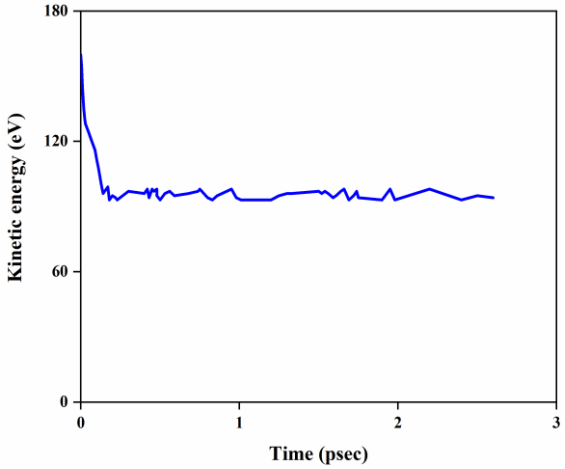

Fig. 2. *Average kinetic energy as a function of time for a 250 eV cascade in gold using the Morse potential*

Figure 3 shows the velocity distribution at 0.26, 0.52 and 2.0 psec. It is clear that the velocity distribution of moving atoms can change and gradually approaches the Maxwell Boltzmann distribution. It is observed that from the initial stage of the cooling phase, the system is strongly deviated from thermal equilibrium, while, at top stage of the cooling phase, equilibrium velocity distribution has been almost established.

The velocity distribution of the central region is almost close to the Maxwell Boltzmann distribution as shown in Figure 4. However, statistics is not enough to give a smooth curve. This result is calculated using the adiabatic molecular dynamics system where electronic contribution to dissipation of thermal energies in cascades is not considered. Since in noble metals as gold, the contribution is small due to weak coupling of the electronic system with the lattice. Thus, Figure 5 does not indicate an equilibration between the electronic and lattice systems. However, this figure seems to imply that at least, local temperature of the lattice system can be described even at such an early stage of the cooling phase of cascade evolution.

THE ANNALS OF "DUNAREA DE JOS" UNIVERSITY OF GALATI
FASCICLE IX. METALLURGY AND MATERIALS SCIENCE
Nº. 4 - 2020, ISSN 2668-4748; e-ISSN 2668-4756
Article DOI: https://doi.org/10.35219/mms.2020.4.02

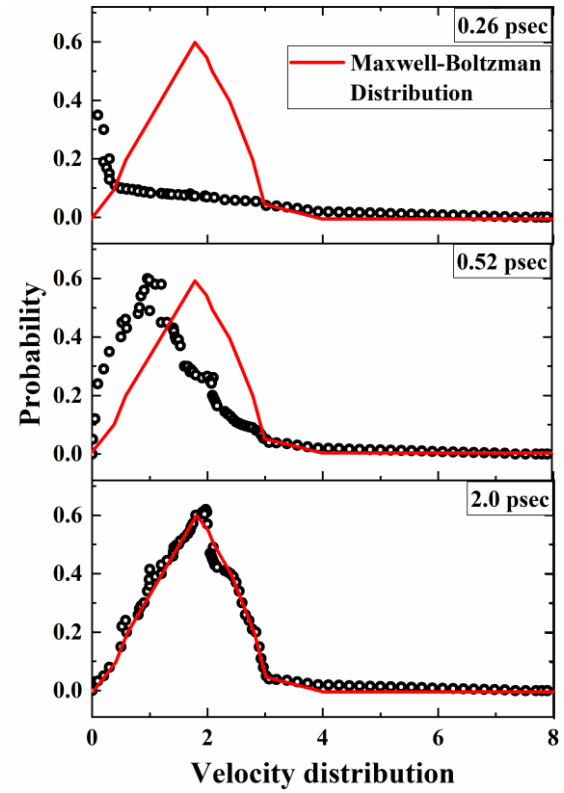

Fig. 3. *Velocity distribution during the cooling phase of cascade for three different times*

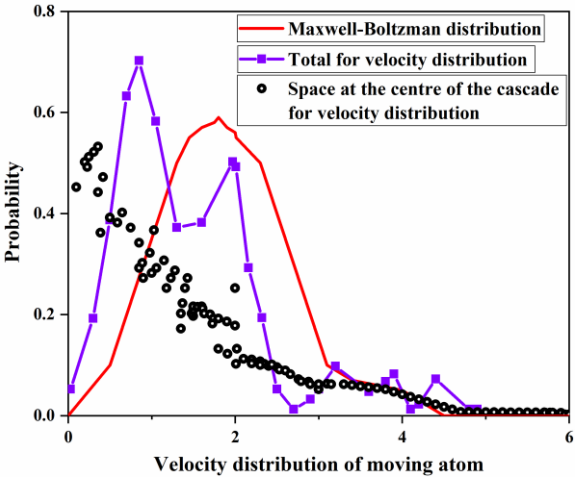

Fig. 4. *A Comparison of velocity distributions during the cooling phase of cascade at 0.4 psec*

4. Conclusions

In this study, the primary states of cascade damage processes are simulated to study the cooling phase, using the molecular dynamics calculation at 250 eV in gold. At early stage in cascade cooling phase, the total kinetic energy remains constant due to the thermally insulated system, the velocity distribution of moving atoms can change and gradually approaches the equilibrium distribution. Local equilibrium of the lattice is established, indicating that the simple jump processes of defects may be applied to the simulation of cascade evolution after the collisional phase. Accordingly, more work could be done by using extremely high energy, temperature and more metals.

References

[1]. Nordlund K., Zinkle S. J., Sand A. E., Granberg F., Averback R. S., Stoller R. E., *et al.*, *Primary radiation damage: A review of current understanding and models*, Journal of Nuclear Materials, 512, p. 450-79, 2018.

[2]. Krasheninnikov A., Nordlund K., *Ion and electron irradiation-induced effects in nanostructured materials*, Journal of applied physics, 107 (7), p. 3, 2010.

[3]. Zwicknagel G., *Molecular dynamics simulations of the dynamics of correlations and relaxation in an OCP*, Contributions to Plasma Physics, 39 (1-2), p. 155-8, 1999.

[4]. Heermann D. W., *Computer-simulation methods. Computer Simulation Methods in Theoretical Physics*, Springer, p. 8-12, 1990.

[5]. Gibson J., Goland A. N., Milgram M., Vineyard G., *Dynamics of radiation damage*, Physical Review, 120 (4), p. 1229, 1960.

[6]. Antoshchenkova E., Luneville L., Simeone D., Stoller R. E., Hayoun M., *Fragmentation of displacement cascades into subcascades: A molecular dynamics study*, Journal of Nuclear Materials, 458, p. 168-75, 2015.

[7]. Bacon D. J., de la Rubia T. D., *Molecular dynamics computer simulations of displacement cascades in metals*, Journal of Nuclear Materials, 216, p. 275-90, 1994.

[8]. Weber W. J., Zhang Y., *Predicting damage production in monoatomic and multi-elemental targets using stopping and range of ions in matter code: Challenges and recommendations*, Current Opinion in Solid State and Materials Science, 23 (4), p. 100757, 2019.

[9]. Stoller R. E., Toloczko M. B., Was G. S., Certain A. G., Dwaraknath S., Garner F. A., *On the use of SRIM for computing radiation damage exposure, Nuclear instruments and methods in physics research section B: beam interactions with materials and atoms*, 310, p. 75-80, 2013.

[10]. Qadr H. M., *Radiation damage and dpa in iron using mcnp5*, European Journal of Materials Science and Engineering, 5 (3), p. 109-14, 2020.

[11]. Qadr H., *Effect of Ion Irradiation on the Mechanical Properties of High and Low Copper*, Atom Indonesia, 46 (1), p. 47-51, 2020.

[12]. Qadr H., *Effect of ion irradiation on the hardness properties of Zirconium alloy*, Annals of the University of Craiova, Physics, 29, p. 68-76, 2019.

[13]. Qadr H. M., Hamad A. M., *Mechanical Properties of Ferritic Martenstic Steels: A Review*, Scientific Bulletin of Valahia University-Materials and Mechanics, 17 (16), p. 18-27, 2019.

[14]. Hiwa M., Ari M., *Investigation of long and short term irradiation hardening of P91 and P92 ferritic/martensitic steels*, Вопросы атомной науки и техники Серия: Термоядерный синтез, 42 (2), p. 81-8, 2019.

[15]. Hiwa M., *Stopping power of alpha particles in helium gas*, Вестник Московского государственного технического университета им НЭ Баумана Серия «Естественные науки», 2 (89), p. 117-25, 2020.

[16]. Arouche TdS., Cavaleiro R. MdS., Tanoue P. S. M., Pereira T. Sd. S., Neto A. Md. J. C., *Heavy Metals Nanofiltration Using Nanotube and Electric Field by Molecular Dynamics*, Journal of Nanomaterials, 2020.

[17]. Gaillac R., Pullumbi P., Bennett T. D., Coudert F.-X., *Structure of Metal-Organic Framework Glasses by Ab Initio Molecular Dynamics*, Chemistry of Materials, 2020.
[18]. Zheng F., Wang L.-W., *Exploring non-adiabaticity to CO reduction reaction through ab initio molecular dynamics simulation*, APL Materials, 8 (4), p. 041115, 2020.
[19]. Ohmura I., Morimoto G., Ohno Y., Hasegawa A., Taiji M., *MDGRAPE-4: a special-purpose computer system for molecular dynamics simulations*, Philosophical Transactions of the Royal Society A: Mathematical, Physical and Engineering Sciences, 372 (2021), p. 20130387, 2014.
[20]. Sheel T., Yasuoka K., Obi S., *Fast vortex method calculation using a special-purpose computer*, Computers & fluids, 36 (8), p. 1319-26, 2007.
[21]. Ackland G., Tichy G., Vitek V., Finnis M., *Simple N-body potentials for the noble metals and nickel*, Philos Mag A, 56 (6), p. 735-56, 1987.
[22]. Torrens I., *Interatomic potentials*, Elsevier, 2012.

THE ANNALS OF "DUNAREA DE JOS" UNIVERSITY OF GALATI
FASCICLE IX. METALLURGY AND MATERIALS SCIENCE
No. 4 - 2020, ISSN 2668-4748; e-ISSN 2668-4756
Article DOI: https://doi.org/10.35219/mms.2020.4.03

MATHEMATICAL MODELING OF THE GRAPHITIZATION PROCESS APPLIED TO NODULAR CAST IRON PARTS

Elisabeta VASILESCU, Marian-Iulian NEACȘU
"Dunarea de Jos" University of Galati, Romania
e-mail: elisabeta.vasilescu@ugal.ro

ABSTRACT

Used mainly in the construction of automobiles as a substitute for steel, or in the metallurgical industry, mainly in the manufacture of rolling mill cylinders, the mechanical properties of nodular cast iron depend largely on their structure, consisting of a ferritic metal mass, ferrite - pearlitic mass or pearlitic and graphite formations (graphite nodules) of maximum compactness.

The modification of the structure in the desired direction of use properties, possible by applying appropriate heat treatments, can be achieved in conditions of technical and economic efficiency by applying the optimal heat treatment variant, in which the technological parameters temperature - time have a decisive influence.

The paper summarizes some research results that aimed to establish the influence of annealing temperature and maintenance time to determine the optimal variant of graphite annealing heat treatment. Process modeling by statistical methods, indicated in the analysis of complex technological processes, has allowed, based on a preliminary experiment and then on the factorial experiment, the establishing of the degree of connection between the technological parameters of the process, as well as the technological parameter with the greatest influence on the process.

KEYWORDS: nodular graphite cast iron, annealing, ferritization, pearlitization, mechanical properties, mathematical modeling

1. Introduction

Ordinary nodular graphite cast irons are non-alloy cast irons having the following basic chemical composition: 3.4-3.9% C; 2.0-2.5% Si; 0.2-1.5% Mn; max. 0.08% P; max.0.03% S.

Classification and characterization of nodular graphite cast iron taking into account mechanical properties include [1, 2]:

- cast iron with very high plasticity (A5min = 17%); They are unalloyed cast irons with a very low content of manganese, phosphorus and sulphur (e.g. Fgn370-17) characterized by ferritic structure;
- cast iron with high plasticity (A5 = 12-17%) still with ferritic structure but with a lower degree of purity (e.g. Fgn400-12);
- cast irons with medium plasticity, characterized by a ferrite-pearlitic structure (e.g. Fgn450-5 and Fgn500-7);
- cast irons with low plasticity (elongation at break is greater than or equal to 2%) characterized by pearlitic structure (e.g. Fgn600-2 and Fgn700-2).

Higher values of mechanical strength correspond to cast irons with bainitic base metal mass, obtained either by isothermal hardening or by alloying [3]; At the same basic metal mass the ratio Rp0,2 / Rm is higher than for steels, the modulus of elasticity is in the range: 16500-18500 daN/mm^2, and the fatigue strength, superior to cast iron with lamellar graphite, has values in the range: 12-28 daN/mm^2.

Nodular graphite cast irons are obtained by a process of modification of ordinary grey cast irons when mainly graphite spheroidization and primary carbide decomposition take place. The modification of the shape of graphite for spheroidization is done almost exclusively with magnesium or cerium (also called antigraphitizing modifiers), used in metallic form of pre-alloys, or in the form of salts. After the modification for the compaction of graphite, especially when these modifiers are used, the free cementite is also obtained in the structure, a constituent frequently present in the structure of nodular graphite cast iron in thin-walled parts.

THE ANNALS OF "DUNAREA DE JOS" UNIVERSITY OF GALATI
FASCICLE IX. METALLURGY AND MATERIALS SCIENCE
No. 4 - 2020, ISSN 2668-4748; e-ISSN 2668-4756
Article DOI: https://doi.org/10.35219/mms.2020.4.03

The removal of free cementite from the structure can be done either by annealing heat treatment or by a new modification (so-called postmodification) which is done with graphitizing modifiers (e.g. ferrosilicon, ferro-silicon-barium, silico-calcium-barium, silico-calcium-zirconium, etc.) introduced into the cast iron jet during its passage from the modification pot for spheroidisation of graphite into the casting pot. Graphite annealing is aimed at: decomposition of cementite and obtaining ferrite, decomposition of only free cementite or decomposition of only bound cementite [8].

The heat treatment of graphite annealing [4, 5] applied in order to decompose (graphitize) the primary cementite is carried out at a high temperature, close to the malleable annealing temperature, and the cooling is done with cooling rates depending on the desired structure, thus resulting in two variants of graphitization annealing (ferritization graphitization annealing or pearlitization graphitization annealing). Graphitization annealing with ferritization is performed in two subvariants: a variant in which the slow cooling takes place up to about 300 °C followed by air cooling, and the variant with pre-cooling in air up to about 650-700 °C followed by the transition to another oven heated to 760-770 °C, in which a maintenance of 45-90 min is applied, for a ferrite - pearlitic or completely ferritic structure. Graphite annealing with perlitization involves cooling the parts in air (quiet or ventilated) to a temperature of about 450 °C, after which they are placed in an oven at 500-550 °C, maintaining a duration calculated with the practical rule "time and inch" followed from a cooling of 40-50 °C/h up to 300 °C and then in the air. For the decomposition of ledeburitic cementite, the annealing must be done at temperatures of 900-950 °C, for the decomposition of the secondary cementite at lower temperatures, and for the decomposition of eutectoid cementite at temperatures below point A1 (at about 700 °C) [8].

2. Experimental conditions

The experiments were performed in laboratory conditions on grey cast iron samples. Different thermal regimes of graphitization annealing were applied, in different experimental variants and the influence of the basic technological parameters was followed, respectively the influence of the annealing temperature and the maintenance time at the annealing temperature on the physical-mechanical properties of the cast iron samples.

Figure 1 shows the heat cycle (heat treatment diagram) in the variant of graphite annealing with ferritization.

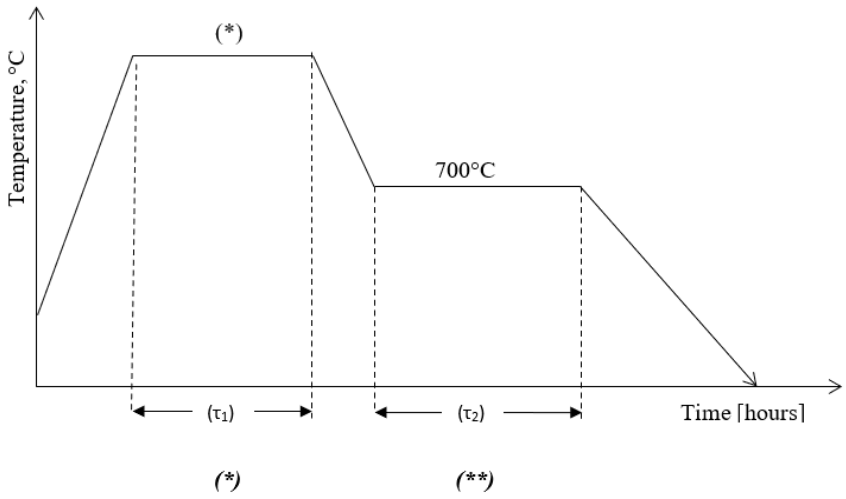

Fig. 1. *Graphitization annealing (thermal cycle) (*) - annealing temperature: 980 °C, 915 °C, 850 °C; ($\tau_1 + \tau_2$) - total holding time: 6 hours (regime 1), 8 hours (regime 2), 10 hours (regime 3), 12 hours (regime 4), 14 hours (regime 5); (**) - oven cooling*

3. Experimental results

Changes in the values of mechanical properties for the experimental heat treatment regimes were analysed. The obtained results are expressed graphically in Figures 2-4.

Modeling in order to establish the equation (equations), respectively the mathematical model of the studied process, is performed based on a preliminary experiment, which provides a priori information, by establishing state variables and process parameters, determining the limits of existence and intervals of variation of factors (process

THE ANNALS OF "DUNAREA DE JOS" UNIVERSITY OF GALATI
FASCICLE IX. METALLURGY AND MATERIALS SCIENCE
No. 4 - 2020, ISSN 2668-4748; e-ISSN 2668-4756
Article DOI: https://doi.org/10.35219/mms.2020.4.03

parameters), establishing the experimental error and the degree of connection between state variables and process parameters [6, 7]. The actual modeling stage that is performed based on a classical or factorial experiment, and the processing of experimental data lead to the obtaining of the mathematical model, a model that describes with some approximation the real process.

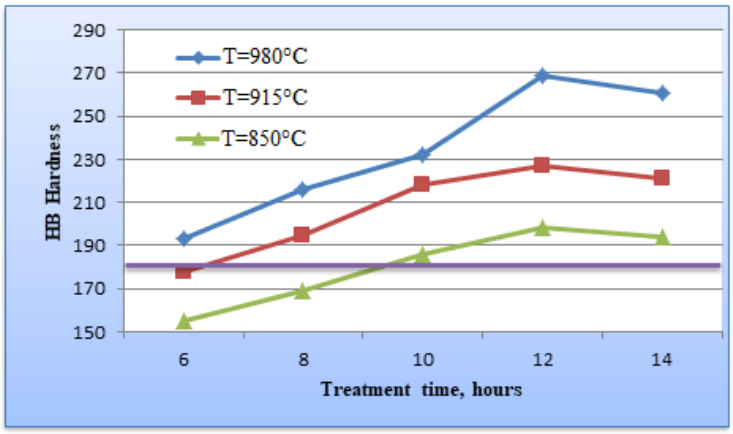

Fig. 2. *Hardness variation (HB) with graphite annealing temperature °C*

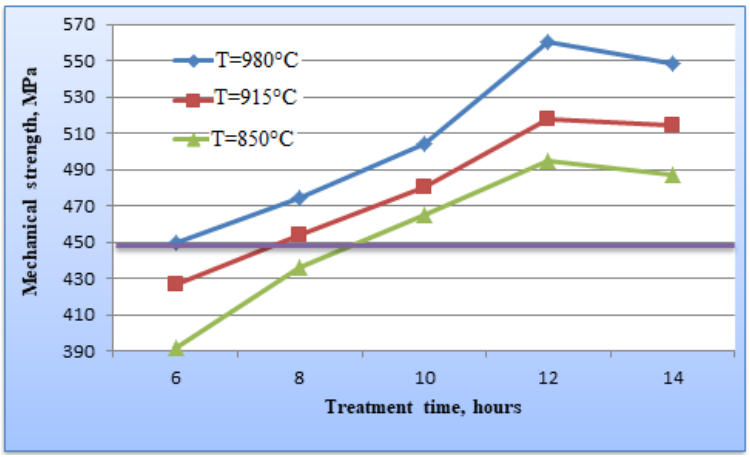

Fig. 3. *Variation of mechanical tensile strength (Rm) with graphite annealing temperature maintenance time*

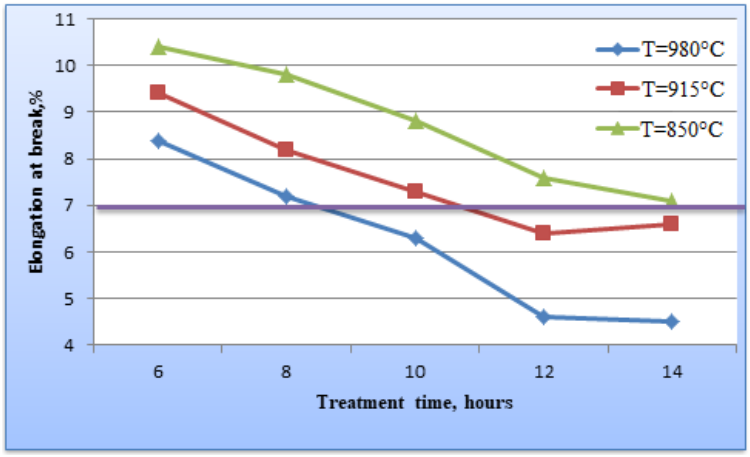

Fig. 4. *Variation of elongation at break (A5) with graphite annealing temperature*

THE ANNALS OF "DUNAREA DE JOS" UNIVERSITY OF GALATI
FASCICLE IX. METALLURGY AND MATERIALS SCIENCE
No. 4 - 2020, ISSN 2668-4748; e-ISSN 2668-4756
Article DOI: https://doi.org/10.35219/mms.2020.4.03

During the thermal processing, according to the adopted variant (graphitization annealing with ferritization), the mechanical properties are influenced by the variation of the treatment time and of the treatment temperature. Cooling rates are constant in the 15 experiments performed.

Mathematical modeling consists in creating a mathematical model that describes the variation of mechanical properties depending on the variation of treatment time and temperature according to the equation:

$$Y = c_0 \cdot x_0 + c_1 \cdot x_1 + c_2 \cdot x_2 + c_{12} \cdot x_1 \cdot x_2$$

For this, it was established:
- higher level (+1),
- basic level (0),
- lower level (-1) and
- the range of variation of the treatment process parameters.

Also, the correspondence of the coded parameters of the time and temperature and their natural parameters was established according to the formula:

$$x_1 = \frac{\tau - \tau_0}{\Delta\tau} \qquad x_2 = \frac{t - t_0}{\Delta t}$$

where: τ - treatment time;
τ_0 - treatment time at the basic level;
t - treatment temperature;
t_0-treatment temperature at baseline.

The correspondence between the values of the factors expressed in natural units and those expressed in coded units is given in Table 1.

Table 1. *Correspondence between the values of the factors expressed in natural units and those expressed in coded units*

Factor	Duration of the process		Annealing temperature	
	Natural units, in hours	Coded values	Natural units, in hours	Coded values
Basic level	$\tau_{(0)} = 10$	$\frac{10-10}{4} = 0$	$t_0 = 915$ °C	$\frac{915-915}{65} = 0$
Variation range	$\Delta\tau = 4$	-	$\Delta t = 65$	-
Higher level	$\tau_{(+1)} = 14$	$\frac{14-10}{4} = +1$	$t_{+1} = 980$ °C	$\frac{980-915}{65} = +1$
Lower level	$\tau_{(-1)} = 6$	$\frac{6-10}{4} = -1$	$t_{-1} = 850$ °C	$\frac{915-850}{65} = -1$

In view of the coded representation of the experiment, the following annotations and symbols were used:

Independent variable:
- X_1 - holding time, τ, [hours];
- X_2 - treatment temperature, t, [°C].

Dependent variables (parameters to be optimized):
- Y_1 - breaking strength, Rm, [MPa];
- Y_2 - Brinell hardness HB;
- Y_3 - specific elongation at break, A5, [%];

Y_i values are expressed in natural units.

The mathematical regression equations are constructed for the 3 studied mechanical properties:

Y_1 - Mechanical resistance;
Y_2 - HB hardness and;
Y_3 - Elongation at break, based on the experimental matrix.

The experimental matrix has the form:

Nr. exp.	X_0	X_1	X_2	$X_1 \cdot X_2$	Y_1	Y_2	Y_3
1	+1	+1	+1	+1	548	261	4.5
2	+1	-1	+1	-1	450	193	8.4
3	+1	+1	-1	-1	514	221	6.1
4	+1	-1	-1	+1	392	155	10.4

THE ANNALS OF "DUNAREA DE JOS" UNIVERSITY OF GALATI
FASCICLE IX. METALLURGY AND MATERIALS SCIENCE
Nº. 4 - 2020, ISSN 2668-4748; e-ISSN 2668-4756
Article DOI: https://doi.org/10.35219/mms.2020.4.03

After calculating the coefficients c_0, c_1, c_2 and $c_1 \cdot c_2$, the following equations expressed in coded quantities for the 3 properties resulted:

$$Y_1 = 476 + 55 \cdot x_1 + 23 \cdot x_2 - 6 \cdot x_1 \cdot x_2;$$
$$Y_2 = 207.5 + 33.5 \cdot x_1 + 19.5 \cdot x_2 + 0.5 \cdot x_1 \cdot x_2;$$
$$Y_3 = 7.35 - 2.075 \cdot x_1 - 0.9 \cdot x_2 + 0.1 \cdot x_1 \cdot x_2$$

By replacing the coded values with the natural ones and performing the calculations, the equations of the mathematical model for the studied (researched) thermal treatment process resulted are:

$$Y_1 = 151.68 + 32.05 \cdot \tau + 0.55 \cdot t - 0.02 \cdot \tau \cdot t;$$
$$Y_2 = -132.4 + 6.54 \cdot \tau + 0.28 \cdot t + 0.02 \cdot \tau \cdot t;$$
$$Y_3 = 27.1 - 0.784 \cdot \tau - 0.016 \cdot t + 0.0003 \cdot \tau \cdot t;$$

As can be seen from the analysis of the mathematical model equations, the mechanical properties are influenced more by the time factor than by the temperature factor because the coefficients of τ are higher than those of temperature.

4. Conclusions

The mechanical properties are influenced by the temperature and the duration of annealing, a significant influence being exerted by the maximum temperature reached at the heat treatment.

The mechanical strength properties (hardness, mechanical tensile strength) increase as the total holding time increases and reach a maximum at a holding time of 12 hours.

Increasing the total maintaining time above this value is no longer effective as the mechanical properties of strength begin to decrease and the mechanical properties of plasticity (elongation at break) remain constant.

References

[1]. Geru N., Chircă D., Bane M., Ripoșan I., ș.a., *Materiale metalice. Structură, proprietăți, utilizări*, Ed. Tehnică, București 1985.
[2]. Sofroni L., Ștefănescu D. M., Vincenz C., *Fonta cu grafit nodular*, Ed. Tehnică, București 1978, p. 5.
[3]. Ripoșan I., Sofroni L., Chișamera M., *Fonta bainitică*, Ed. Tehnică București, 1988.
[4]. Popescu N., Dumitrescu C., Munteanu A., *Tratamente termice și prelucrări la cald*, E. D. P. București, 1983.
[5]. Popescu N., Vitănescu C., *Tehnologia tratamentelor termice*, Ed. Tehnică, București, 1974.
[6]. Taloi D., Bratu C., Florian E., Berceanu E., *Optimizarea proceselor metalurgice*, E. D. P., București, 1983.
[7]. Taloi D., *Optimizarea proceselor tehnologice. Aplicații în metalurgie*, Editura Academiei, București, 1987.
[8]. Geru N., *Metalurgie fizică*, E. D. P. București, 1981.

THE ANNALS OF "DUNAREA DE JOS" UNIVERSITY OF GALATI
FASCICLE IX. METALLURGY AND MATERIALS SCIENCE
Nº. 4 - 2020, ISSN 2668-4748; e-ISSN 2668-4756
Article DOI: https://doi.org/10.35219/mms.2020.4.04

CONSIDERATIONS REGARDING THE EVOLUTION OF THE SOLIDIFIED CRUST AT THE CONTINUOUS CASTING STEEL

Marian BORDEI
"Dunarea de Jos" University of Galati, Romania
e-mail: mbordei@ugal.ro

ABSTRACT

The continuous casting of the steel can cause cracks on the surface or inside, which arise due to thermal and mechanical stresses. To eliminate these defects, mathematical models are drawn up with which temperature fields, expansions and stresses can be determined. The purpose of making these models is to locate the areas with a high risk of cracking so that, finally, the continuous casting machines and working conditions can be modified, so as to eliminate, or at least diminish, the defects. The knowledge of the thermal state of the steel in the continuous casting machine is necessary for the transposition on mathematical bases of the technological process and the elaboration of some simulation models of the solidification, which would allow the optimization of the afferent plant.

The proposed mathematical model takes into account - when studying the heat transfer phenomena in the tundish - the convective motion of the steel, which influences the thickness of the solidified crust and the evolution of the temperature in the section of the continuously cast steel thread.

By running the simulation program were determined the variation of the thickness of the solidified crust as a function of time, overheating in the crystallizer and convection coefficient.

KEYWORDS: continuous casting, thermal state, solidification crust

1. Introduction

The process of continuous casting of semi-finished products is characterized by a number of parameters that condition both the design and construction of specific installations-machinery-equipment, as well as the quality of the products on the flow-casting. In addition to the "classic" processes, more and more efficient manufacturing processes are constantly appearing: casting thin slabs, casting with the deformation of the steel wire in the machine or casting.

The most important difficulties - which must be overcome when adopting such technologies - can be grouped into:

- casting of semi-finished products with minimum defects;
- conservation of thermal energy for the purpose of direct rolling;
- reduction of the thickness of the semi-finished products with or without deformation in the continuous casting installation (with the correlation of their components);
- adaptation of the rolling to the new conditions: direct deformation (with the minimum decrease of the temperature between casting and deformation), reduced corrosion to rolling, etc.

To study the thermal state of continuous cast steel thread, empirical models can be used - obtained by correlating experimental value results with mathematical simulation models. In general, empirical models cannot be extrapolated to conditions other than those for which the experiments were performed, when some parameters (temperature of the steel inside the thread, thickness of the solidified crust, etc.) are difficult to follow. Mathematical models have the advantage that, once verified, they have generalization possibilities.

Kohn and Morillon studied the solidification of steel taking into account the heat exchanges by convection in liquid steel; for this, they considered that the liquid consists in of two media, one - corresponding to the dendritic solidification zone - in which the heat exchanges are made by conduction and the second one - corresponding to the equiaxial solidification zone, the convective displacement of the liquid leading to a constant temperature [1].

THE ANNALS OF "DUNAREA DE JOS" UNIVERSITY OF GALATI
FASCICLE IX. METALLURGY AND MATERIALS SCIENCE
Nº. 4 - 2020, ISSN 2668-4748; e-ISSN 2668-4756
Article DOI: https://doi.org/10.35219/mms.2020.4.04

Tozoshima and Takasashi proposed a model for "semi-solid" materials, by applying Darcy's law to the movement of liquid steel through interdendritic spaces - in the case of the biphasic solid-liquid zone [2].

Miyazawa developed a mathematical model for estimating the solidification profile and slab surface temperature, using the integration of the continuous cast thread section and took into account the different effects of cooling rate and cooling conditions on the upper and lower slabs, respectively.

Although the number of continuous casting machines has increased a lot, however, the complex processes regarding the solidification and cooling of the related semi-finished products are still in the research phase, not being elaborated a unitary model, generally valid for the respective processes.

Taking into account the presented aspects, we proposed a mathematical model for determining the evolution of the crust solidification and heat flux in the tundish, as well as a model for determining the temperature in the continuously cast steel thread - on the path to the exit of the machine.

The alloy used for the research is a general-purpose carbon steel for construction S235J2G4, according to EURONORM 10025 (OL 37-4k, according to STAS 500). The thermophysical parameters of steel solidification were calculated according to studies and research in the literature [3].

2. Theoretical considerations on the convection phenomenon at the solid-liquid interface

The thermal state of liquid steel is characterized by overheating (the difference between the temperature of the steel at a given time - at a given level - and the temperature of the liquid). It is important to know, at different levels of the machine, the thickness of the solidified crust and the temperature distribution in the liquid steel, as well as the temperature of the liquid steel as the solidification front advances.

At the solid-liquid interface (at the boundary of the solidification front) a convection heat transfer takes place. The existence of convective motion can lead to a reduction in the thickness of the solidified crust at the respective level in the tundish, as well as to a significant increase in the temperature on the surface of the product, at the exit of the tundish. For these reasons, it is necessary to take into account the convective motion when studying the heat transfer phenomena in the tundish.

To solve this problem, mathematical analysis solutions can be used for the case of free border systems. The model must allow the numerical evaluation of the thermal state of the steel, in accordance with the experimental results that can be obtained at a certain level of the tundish, during an industrial casting. In order to reduce the perforations, a sufficiently thick and uniform solid crust must be ensured at the exit of the tundish.

3. Results obtained

Based on the mathematical relationships in the literature, the variation of the solidified crust of continuously cast steel was determined [5]. By running the program, the variations of the thermophysical parameters depending on the temperature characteristic of the studied steel were determined (Figures 1-4), respectively, the variation of the thickness of the solidified crust as a function of time.

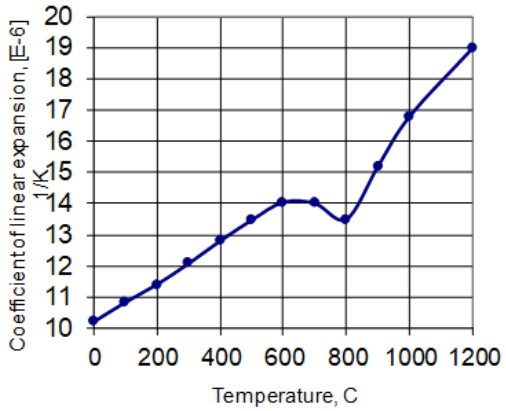

Fig. 1. *Variation of the coefficient of linear expansion of steel as a function of temperature*

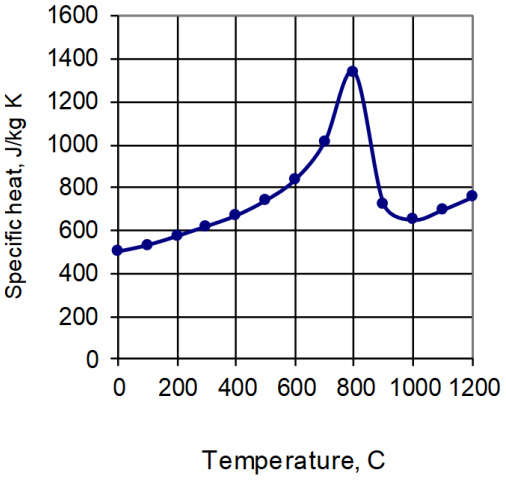

Fig. 2. *Variation of specific heat of steel as a function of temperature*

THE ANNALS OF "DUNAREA DE JOS" UNIVERSITY OF GALATI
FASCICLE IX. METALLURGY AND MATERIALS SCIENCE
Nº. 4 - 2020, ISSN 2668-4748; e-ISSN 2668-4756
Article DOI: https://doi.org/10.35219/mms.2020.4.04

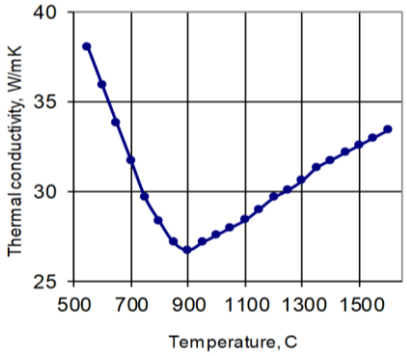

Fig. 3. *Variation of thermal conductivity of steel as a function of temperature*

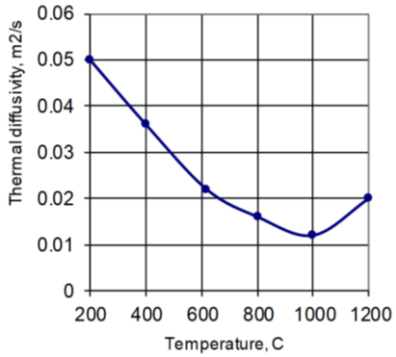

Fig. 4. *Variation of the thermal diffusivity coefficient of the steel as a function of temperature*

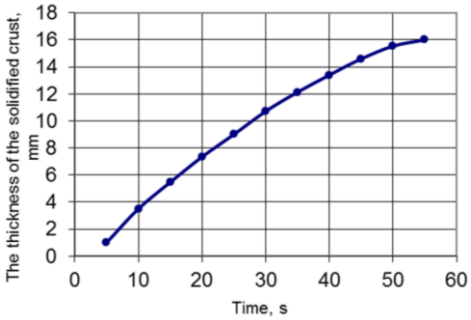

Fig. 5. *Variation of the crust thickness solidified over time*

4. Conclusions

Following the analysis of the diagrams obtained by calculation with the mathematical model used, some conclusions can be drawn that contribute to the understanding of the phenomena that take place in the tundish and to the optimization of the parameters of the solidification process of the continuously cast slabs.

The thickness of the solidified crust increases - along the path in the tundish - being favored by the following factors:

- the lower the overheating is;
- with the decrease of the convection coefficient;
- with the decrease of the casting speed.

References

[1]. ***, *Continuous Casting*, vol. 1-9, Iron and Steel Society, 186 Thorn Hill Road, Warrendale, PA 15086-7512, 1979-1997.

[2]. ***, Modeling of Casting and Welding Processes, Conference Series, vols. 1-10, TMS, Warrendale, PA.

[3]. ***, *Continuous Casting, in the Making, Shaping, and Treating of Steel*, vol. 2, A. Cramb, ed. Pittsburgh, PA: Assoc. of Iron & Steel Engineers, 2003.

[4]. Oprea S., *Corelaţia dintre proprietăţile termofizice şi mecanice ale materialelor metalice cu procesul de încălzire*, Metalurgia, p. 435-445, 7/1973.

[5]. Bordei M., *Considerente privind deformarea plastica a semifabricatelor turnate continuu in scopul optimizarii unor parametri ai proceselor de turnare continua-laminare*, Teză de doctorat, Galati, 1999.

[6]. Bratu V., Mortici C., Oros C., Ghiban N., *Mathematical model of solidification process in steel continuous casting taking into account the convective heat transfer at liquid–solid interface*, Computational Materials Science, vol. 94, November 2014.

[7]. Rogberg B., *Testing and Application of a Computer Program for Simulating the Solidification Process of a Continuous Cast Strand*, Teză de doctorat, Stockholm, 1990.

[8]. Bamberger M., *Mathematical model for the solidification of high-carbon steel in continuos casting*, Iron and Steel International, 2/1977.

[9]. Barber B., *Détermination de la température de surface sur ligne de coulée continue et du transfert thermique lors de la coulée continue*, La Revue de Métallurgie-CIT, 11/1996.

[10]. Bordei M., *Cercetări privind îmbunătăţirea randamentului de metal prin creşterea calităţii tablelor şi benzilor obţinute prin laminarea bramelor turnate continuu*, Contract nr. 67/1996, beneficiar: SIDEX S.A Galaţi.

THE ANNALS OF "DUNAREA DE JOS" UNIVERSITY OF GALATI
FASCICLE IX. METALLURGY AND MATERIALS SCIENCE
N°. 4 - 2020, ISSN 2668-4748; e-ISSN 2668-4756
Article DOI: https://doi.org/10.35219/mms.2020.4.05

CONSIDERATIONS REGARDING THE EVOLUTION OF THE STEEL THERMAL STATE IN THE CONTINUOUS CASTING PLANT

Marian BORDEI
"Dunarea de Jos" University of Galati Romania
e-mail: mbordei@ugal.ro

ABSTRACT

In continuous casting it is very important that the cooling system is correctly dimensioned. Improper cooling conditions can reduce the quality of the finished product and cause perforations of the solidified crust. In order to be able to minimize the occurrence of defects, it is preferable that, under the conditions of a given cooling system, the temperature distribution in the steel wire be known. It is also necessary to know the thickness of the solidified crust, especially immediately below the crystallizer, because a thin crust at this level can be perforated due to the ferrostatic pressure of the steel. The knowledge of the thermal state of the steel in the continuous casting installation is necessary for the transposition on mathematical bases of the technological process and the elaboration of some models of simulation of the solidification, which would allow to optimize the operation of the afferent installations.

By considering the convection motion can be explained the influence of electromagnetic agitation and deformation of the steel wire on the incompletely solidified area on the quality and structure of cast steels; convective currents reduce overheating, which leads to a decrease in columnar crystallization in favour of axial crystallization. By running the simulation program were determined the variation of the thermal flux at different levels in the tundish, as well as the evolution of the temperature at the surface of the continuously cast steel thread.

KEYWORDS: continuous casting, solidification process, mathematical model

1. Theoretical considerations

Mathematical simulation models render the thermal field of the continuously cast steel thread as a function of some process parameters: casting speed, steel overheating, thermophysical properties of the tundish material, steel quality, tundish geometry, etc.

Some important operational variables such as: tundish length, cooling system, metallurgical length and casting speed - are conditioned by the heat transfer during the process. The quality of the semi-finished product is significantly influenced by the speed of heat extraction, excessive cooling leading to cracks, swelling of the thread, large columnar areas, etc.

Because thermal conductivity has a major role in the process of continuous casting, on its base, several mathematical models have been developed, and they were used to analyse the stresses that are formed when the crust solidifies; they contribute to the understanding of the causes of surface defects and internal cracks. They are used to improve cooling systems, casting technologies and process control.

Hills and Mizikar are among the first authors who wrote about the modeling of the heat flow in the continuous casting system. Hills [1] used a thermal balance method to solve the problem of thermal conductivity and solidification in a complex system, such as continuous casting; he neglected the conductivity of the steel in the direction of the thread flow and considered the overheating in the liquid area to be zero.

Mizikar [2] applied the finite element method to develop the two-dimensional heat conduction equation for continuously cast slabs. He also developed the one-dimensional conductivity transfer equation, Fourier type, for a moving element - from the meniscus to the exit of the machine - predicting the temperature distribution along the length of the continuous cast thread. He integrated the convective aspect of heat transfer from the liquid into a model based on the conductivity of steel by increasing the conductivity coefficient.

THE ANNALS OF "DUNAREA DE JOS" UNIVERSITY OF GALATI
FASCICLE IX. METALLURGY AND MATERIALS SCIENCE
Nº. 4 - 2020, ISSN 2668-4748; e-ISSN 2668-4756
Article DOI: https://doi.org/10.35219/mms.2020.4.05

Many of the continuous casting machines are designed based on experience, on models established through simulations and tests, and on empirical relationships. The management of the continuous casting process is, in many cases, based on models with low applicability.

The alloy used for the research is a general-purpose carbon steel for construction S235J2G4, according to EURONORM 10025 (OL 37-4k, according to STAS 500). The thermophysical parameters of steel solidification were calculated according to studies and research in the literature [3].

2. Results obtained

The temperature field in the continuous cast thread can be represented by the fundamental equation of thermal conductivity (Fourier equation). Based on the data from the program, the relations used for the calculation of the main parameters that give the thermal state of the continuously cast steel thread were determined.

Running the program, it was determined: the variation of solidified crust thickness as a function of time, the overheating in the tundish and the convection coefficient (Figures 1, 2), the variation of the thermal flux at different levels in the tundish (Figure 3), as well as the surface temperature evolution. of continuously cast steel thread (Figure 4) [4].

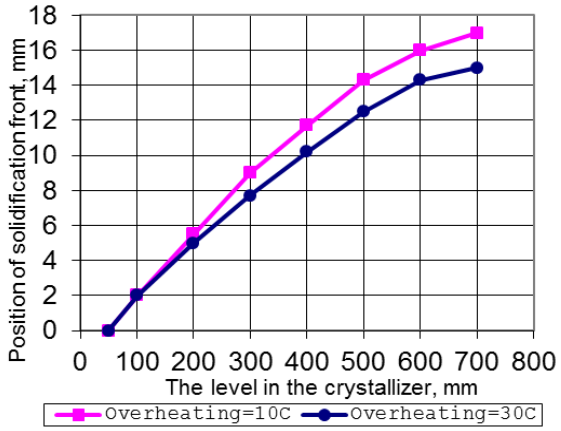

Fig. 1. *The thickness of the crust solidified at different levels in the tundish for two values of steel overheating*

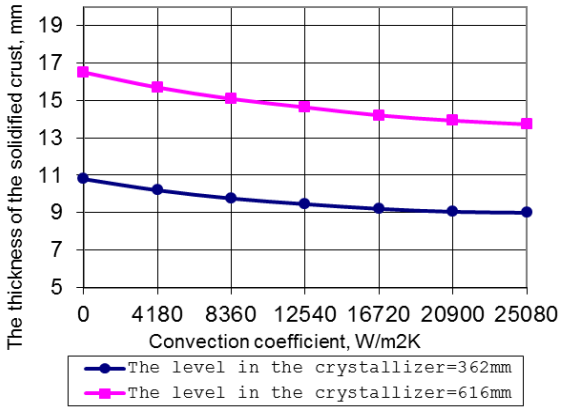

Fig. 2. *The variation of the solidified crust thickness depending on the convection coefficient at different levels in the tundish*

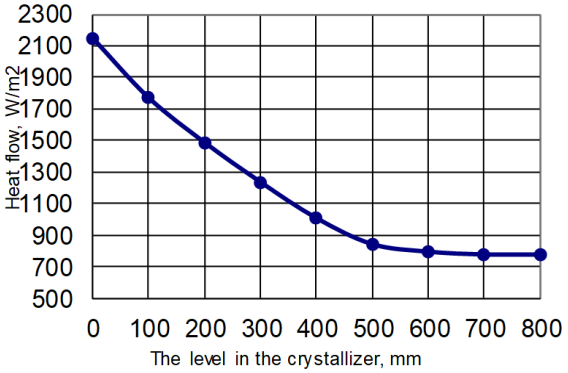

Fig. 3. *Variation of heat flux at different levels in the tundish (v = 1 m/min)*

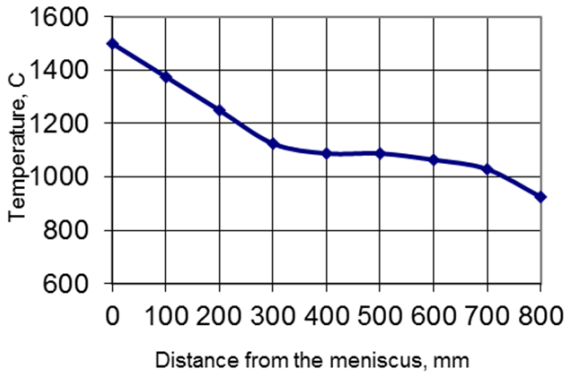

Fig. 4. *Temperature distribution at the surface of the steel thread, in the middle of the face (v = 1 m/min)*

3. Interpretation of results

The highest heat flux density occurs in the meniscus (Figure 3), the fall that follows is explained by the following mechanism:

THE ANNALS OF "DUNAREA DE JOS" UNIVERSITY OF GALATI
FASCICLE IX. METALLURGY AND MATERIALS SCIENCE
Nº. 4 - 2020, ISSN 2668-4748; e-ISSN 2668-4756
Article DOI: https://doi.org/10.35219/mms.2020.4.05

- by increasing the crust of the steel thread, the ferrostatic pressure exerted on the wall of the tundish decreases, the heat transfer worsens;

- by decreasing the temperature of the thread surface, the contraction is increased (shrinkage of the thread crust), fact that contributes to the amplification of the mentioned effect;

- the growing crust of the thread worsens the heat flux discharged from the tundish due to low temperature gradients and increasing thermal resistivity.

The cooling curve in Figure 4, calculated at an extraction speed of 1 m/min, shows the temperature drop from the beginning of the casting process (solidification), in this phase there is still a good heat transfer between the thread surface and the tundish. As the casting process continues, the heat transfer worsens, the cause being mainly the increase of the gap between the tundish and the solidified crust, as well as the modification of the thermal conductivity properties of the slag film. Given that the heat flux from the surface of the thread to the tundish is now lower than that coming from inside the thread, a slight increase in temperature is reached at the surface of the thread.

References

[1]. Bamberger M., *Mathematical model for the solidification of high-carbon steel in continuous casting*, Iron and Sleel International, 2/1977.

[2]. Braun H., *Computersimulation thermischer und mecanischer Vorgänge beim Brammenstranggieben von Stahl*, Stahl und Eisen, p. 79-85, 9/1996.

[3]. Oprea S., *Corelaţia dintre proprietăţile termofizice şi mecanice ale materialelor metalice cu procesul de încălzire*, Metalurgia, p. 435-445, 7/1973.

[4]. Bordei M., *Considerente privind deformarea plastica a semifabricatelor turnate continuu in scopul optimizarii unor parametri ai proceselor de turnare continua-laminare*, Teză de doctorat, Galati, 1999.

[5]. ***, *Continuous Casting*, vol. 1-9, Iron and Steel Society, 186 Thorn Hill Road, Warrendale, PA 15086-7512, 1979-1997.

[6]. ***, *Modeling of Casting and Welding Processes*, Conference Series, vols. 1-10, TMS, Warrendale, PA.

[7]. ***, *Continuous Casting, in The Making, Shaping, and Treating of Steel*, vol. 2, A. Cramb, ed. Pittsburgh, PA: Assoc. of Iron & Steel Engineers, 2003.

[8]. Bratu V., Mortici C., Oros C., Ghiban N., *Mathematical model of solidification process in steel continuous casting taking into account the convective heat transfer at liquid–solid interface*, Computational Materials Science, vol. 94, November 2014.

[9]. Oprea S., *Corelaţia dintre proprietăţile termofizice şi mecanice ale materialelor metalice cu procesul de încălzire*, Metalurgia, p. 435-445, 7/1973.

[10]. Rogberg B., *Testing and Application of a Computer Program for Simulating the Solidification Process of a Continuous Cast Strand*, Teză de doctorat, Stockolm, 1990.

[11]. Bamberger M., *Mathematical model for the solidification of high-carbon steel in continuos casting*, Iron and Sleel International, 2/1977.

[11]. Barber B., *Détermination de la température de surface sur ligne de coulée continue et du transfert thermique lors de la coulée continue*, La Revue de Métallurgie-CIT, 11/1996.

[12]. Bordei M., *Cercetări privind îmbunătăţirea randamentului de metal prin creşterea calităţii tablelor şi benzilor obţinute prin laminarea bramelor turnate continuu*, Contract nr. 67/1996, beneficiar: SIDEX S.A Galaţi.

THE ANNALS OF "DUNAREA DE JOS" UNIVERSITY OF GALATI
FASCICLE IX. METALLURGY AND MATERIALS SCIENCE
No. 4 - 2020, ISSN 2668-4748; e-ISSN 2668-4756
Article DOI: https://doi.org/10.35219/mms.2020.4.06

OBTAINING AND CHARACTERIZING PHOSPHATIC PORCELAIN

Florentina POTECASU, Petrică ALEXANDRU
"Dunarea de Jos" University of Galati, Romania
e-mail: florentina.potecasu@ugal.ro

ABSTRACT

The research aimed to obtain phosphate porcelain, by using the ash resulting from burning bones from meat processing plants. The applied processing technology allows obtaining fine ceramics at lower temperatures than the one used in the case of feldspar porcelain, having as effect the increase of the durability of the firing furnaces and the realization of the products at lower production costs. Five series of phosphate porcelain samples were performed in laboratory conditions, with different compositions, by firing at a temperature of 1250 °C, temperatures lower than those necessary for the firing of feldspar porcelain of 1350-1450 °C. The porosity and density of the samples were determined and the microstructural analysis of the materials made in the five research variants was made.

KEYWORDS: phosphate porcelain, kaolin, quartz, porosity, density, microstructural analysis

1. Introduction

The notion of pottery has retained its original meaning given by the word "keramos", which in ancient Greek meant the land of the potter and his pots [1-5]. Over time, however, this notion has gained a broader meaning, encompassing all pottery and porcelain products obtained by burning ceramic masses, both domestic, utilitarian or decorative, and industrial [6-9]. Modern ceramics has industrial applications in high temperature areas in the electrical, nuclear, space, etc. With such materials, the shuttles that cross the cosmic space are lined, car engines are made, the entrails of the earth are drilled or the human bone is replaced in difficult surgical operations [8-13].

Over time, aesthetic education through ceramics has left its mark on people. It is felt spontaneously since childhood, due to the daily contact with the surrounding ceramic objects, in different hypostases. Porcelain, as a technical material, has very valuable properties: high mechanical and electrical resistance, chemical and thermal stability, as well as exceptional ornamental possibilities. The structurally component elements of the porcelain material unevenly influence the strength, white colour, transparency and other properties [6, 8, 9]. Porcelain, nicknamed in German as "Weißes Gold" (white gold), is a white and translucent ceramic material obtained by burning at high temperatures a paste composed of quartz, kaolin and feldspar together with smaller additions of other components. It is used in the manufacture of industrial or laboratory vessels, electrical insulators, household vessels or decorative objects. According to the ratio of the components it can be classified as hard porcelain or soft porcelain. For classic hard porcelain the ratio between kaolin, feldspar and quartz is 50/25/25, while for soft porcelain it is about 30/30/40 [14].

The structure of the porcelain material and its most important properties are determined both by the quantitative properties of the material components and by the firing regime, i.e., the firing temperature and duration, as well as the character of the atmosphere from different firing periods [6, 9].

Phosphate porcelain is a special type of soft paste porcelain, called "oschina", because its main component is bone ash; was discovered in Staffordshire in the late 1700s and was adopted by most English factories in the early 1800s [6, 8]. The precise ratios between the components as well as the processing technology are not completely known.

Phosphate porcelain is part of the oxide system RO - Al_2O_3 - SiO_2 - P_2O_5. By converting total RO to CaO, its composition can be located in the domain around the eutectic corresponding to the tricalcium phosphate-anorthite-silicon dioxide subsystem [Ca_3 (PO_4) 2 - $CaAl_2Si_2O_8$ - SiO_2]. Phosphate porcelain is characterized by a high content of glassy phase; in the vitreous matrix there is a distribution, especially, of

THE ANNALS OF "DUNAREA DE JOS" UNIVERSITY OF GALATI
FASCICLE IX. METALLURGY AND MATERIALS SCIENCE
Nº. 4 - 2020, ISSN 2668-4748; e-ISSN 2668-4756
Article DOI: https://doi.org/10.35219/mms.2020.4.06

tricalcium and anorthite phosphate crystals and to a small extent quartz.

2. Experimental research

The research aimed at carrying out in laboratory conditions a series of phosphate porcelain samples symbolized R1, R2, R3, R4, R5. To obtain phosphate porcelain, the basic raw material is the calcined bones meal, which represents 35-60% of the gross mass (the final preparation is done by degreasing but also by removing gelatin and Fe oxides).

Five series of samples with different compositions were performed in laboratory conditions:

R1 - Kaolin 25%; Feldspar 20%; Quartz 15%; 40% bone ash.

R2 - 25% kaolin; Feldspar 13%; Quartz 12%; 50% bone ash.

R3 - Kaolin 20%; Feldspar 15%; Quartz 15%; 50% bone ash.

R4 - 40% kaolin clay; Feldspar 20%; 40% bone ash.

R5 - 30% kaolin clay; Feldspar 15%; Quartz 5%; 50% bone ash.

Feldspar is a very common silicate, having the chemical composition (Ba, Ca, Na, K, NH_4) (Al, B, Si) 4O8 (the elements in parentheses can be substituted for each other). The crystallization system for this mineral is monoclinic or triclinic, with a hardness of 6-6.5.

Kaolin is a clay (rock) composed mostly of the mineral kaolinite. Kaolin has a fine granulation (<2 μm), free of iron oxides, white in colour. Kaolin is a rock with a very fine grain, with a low plasticity, but with high resistance to high temperatures, by burning it becomes solid and very compact (dense).

Quartz (silicon dioxide) is a mineral spread in the earth's crust, which has the chemical composition of SiO_2 crystallizing in the trigonal system. In its pure state, quartz is colourless, the impurities in the crystal determine the colour of the mineral. Quartz frequently crystallizes in gaps in rocks called geodes. The cleavage is non-existent, the crack has a pearly colour, reaches a value of 7 on the Mohs hardness scale.

Phosphate porcelain - according to what has been mentioned above, is part of the oxide system RO - Al_2O_3 - SiO_2 - P_2O_5. Its place in this system - converting total RO to CaO, can be circumscribed to the domain located around the eutectic corresponding to the tricalcium phosphate-anorthite-silicon dioxide subsystem. Phosphate porcelain is characterized by a high glassy phase content; in the vitreous matrix there is a distribution, especially, of tricalcium and anorthite phosphate crystals and to a small extent quartz. Its porosity is very low (1% closed pores).

Phosphate porcelain is characterized by a short glazing interval, which introduces difficulties in the firing of the biscuit (it uses a glaze based on boric frit, easily fusible, applied on products heated to 40-50 degrees C; the second firing must be conducted so as to ensure a good melting and spreading of the glaze.

The porcelain structure consists of:

- isotropic glass mass composed of feldspar glass, with a varying degree of saturation in Al_2O_3 and SiO_2;
- undissolved and molten particles, as well as dissolved by Al_2O_3 and SiO_2;
- mullite crystals $3Al_2O_3 \cdot 2SiO_2$.

Another very important element in the structure of the porcelain mass are the pores, which decrease the quality of the porcelain and cannot be completely removed. Porosity occurs on drying after removal of mechanically distributed water, as well as hygroscopic water from the clay substance, during the initial firing period. The mass has the highest porosity, of about 35...40%, before the beginning of vitrification, when the firing is up to 1000...1050 °C. As the glass mass forms, the pores fill, the products shrink, the porosity decreases, the mass becomes more compact.

Depending on the temperature and duration of firing, the process of dissolving Al_2O_3 and SiO_2 in feldspar glass can be more or less complete and therefore the amount and composition of feldspar glass in porcelain mass can vary widely (Fig. 1).

The mass-formed mullite crystals replace in the feldspar glass the granules dissolved by the clay and quartz, thus ensuring the further development of the glass mass and the improvement of the technical indices necessary for the manufacture of insulators and other categories of technical porcelain.

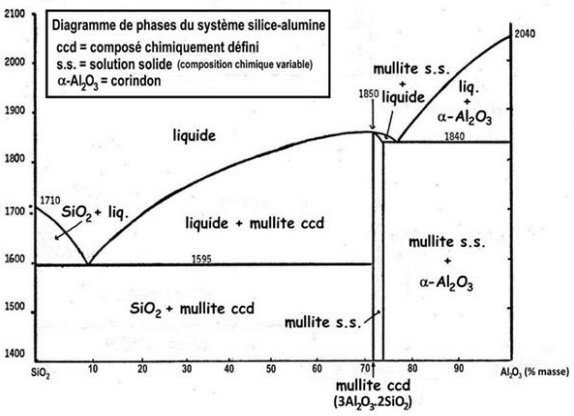

Fig. 1. *The binary diagram SiO_2-Al_2O_3*

An important structural part of porcelain are the quartz granules and undissolved clay substances in the feldspar glass, which together with the crystals of the mullite form the skeleton of the mass, ensuring

THE ANNALS OF "DUNAREA DE JOS" UNIVERSITY OF GALATI
FASCICLE IX. METALLURGY AND MATERIALS SCIENCE
Nº. 4 - 2020, ISSN 2668-4748; e-ISSN 2668-4756
Article DOI: https://doi.org/10.35219/mms.2020.4.06

the preservation of the forms produced in the final firing period. The mass remains from 60...85% unmodified quartz.

Another structural element of porcelain are crystalline aluminosilicates, which are formed during firing. When the porcelain is fired, the mullite $3Al_2O_3 \cdot 2SiO_2$ is formed (Fig. 1) and not the silimanite $Al_2O_3 \cdot SiO_2$, as it was assumed before the researches.

The mullite has several valuable properties: high melting start temperature (about 1810 °C), high mechanical and electrical resistance, chemical stability, low coefficient of thermal expansion and high thermal stability. The formation of mullite crystals is observed even at a temperature of about 1250 °C.

The research followed two main stages:

- obtaining samples from phosphate porcelain with different compositions, in laboratory conditions, by firing at a temperature of 1250 °C, a temperature lower than that required for firing feldspar porcelain of 1350-1450 °C.
- characterization of the porcelain samples obtained, by determining the porosity, density and analysis under an optical microscope.

3. Working procedure

In order to achieve the objectives in obtaining samples of phosphate porcelain with different compositions in laboratory conditions, we proceeded as follows:

Kaolin, feldspar, quartz, bone ash and kaolin clay were used as raw materials. Kaolin, feldspar, quartz and kaolin clay being in a powder state, except for bone ash obtained by grinding calcined pork bones at a temperature of 800 ºC (Fig. 2). With the help of a mortar, we crushed the bones that were burned and calcinated previously.

a. b.

Fig. 2. *Appearance of burnt pork bones at a temperature of 300-400 ºC (left side) and calcined bones at a temperature of 800 ºC (right side)*

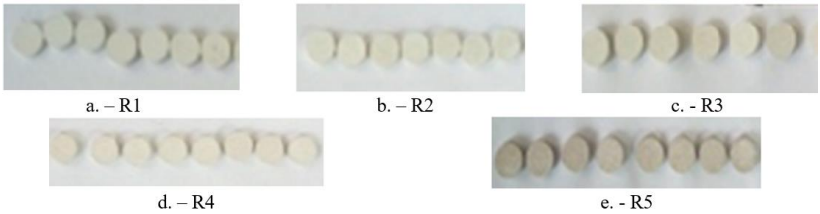

Fig. 3. *Samples obtained by pressing*

3.1. Porosity and density of samples

Porosity was determined by water absorption.

$$P = \frac{\Delta m}{m_0} * 100\ [\%]$$

The pressed samples were fired in an electric oven at 1250 °C for 2.5 hours, according to the diagram in Figure 4.

After firing, the samples were weighed and measured to determine density, then immersed in boiling water, kept for one hour and then wiped and weighed to determine porosity.

We obtained samples in the form of pills with a diameter of 12.2 mm and a height between 2.4 and 3.2 mm. The pressing force for all samples was the same, namely 10 kN, resulting in a compaction pressure of 85 MPa. After pressing, the samples were measured and weighed and determined for the 5 series of porosity and density (Tables 1 and 2).

With the results of the performed determinations, the histograms from Fig. 5 and 6 were made.

THE ANNALS OF "DUNAREA DE JOS" UNIVERSITY OF GALATI
FASCICLE IX. METALLURGY AND MATERIALS SCIENCE
N°. 4 - 2020, ISSN 2668-4748; e-ISSN 2668-4756
Article DOI: https://doi.org/10.35219/mms.2020.4.06

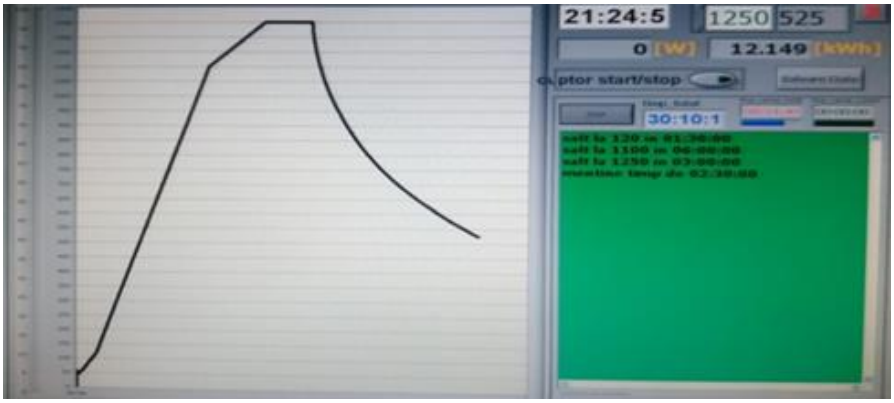

Fig. 4. *Firing diagram*

Table 1. *Determination of sample porosity*

Composition	m_0 [g]	m_1 [g]	Δm [g]	Porosity $\frac{\Delta m}{m_0}$*100[%]
R1	0.70	0.76	0.06	8.57
R2	0.65	0.71	0.06	9.23
R3	0.67	0.72	0.05	7.46
R4	0.67	0,68	0.01	1.49
R5	0.61	0.63	0.02	3.28

m_0 - mass of the porcelain sample after firing at 1250 °C.
m_1 - the mass of the sample after being kept in boiled water for one hour.

Table 2. *Determination of sample density*

Composition	m_0 [g]	d [mm]	h [mm]	V [cm^3]	ρ [g/cm^3]
R1	0.70	12.1	2.8	0.327	2.14
R2	0.65	12.1	2.6	0.305	2.13
R3	0.67	11.9	2.7	0.308	2.17
R4	0.67	11.8	2.6	0.288	2.32
R5	0.61	11.75	2.5	0.268	2.27

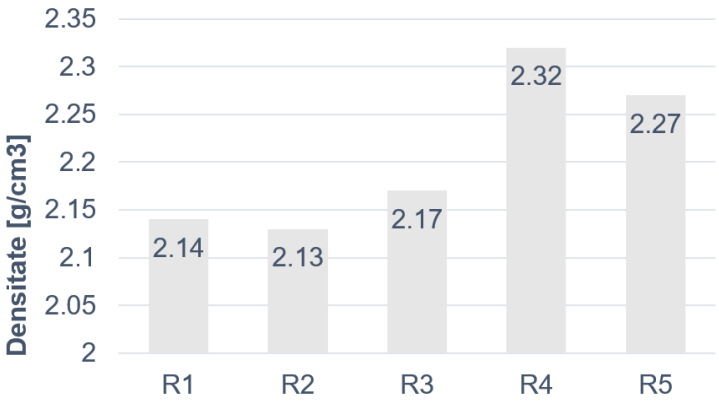

Fig. 5. *Density depending on the composition of the porcelain mass fired at a temperature of 1250 °C*

THE ANNALS OF "DUNAREA DE JOS" UNIVERSITY OF GALATI
FASCICLE IX. METALLURGY AND MATERIALS SCIENCE
Nº. 4 - 2020, ISSN 2668-4748; e-ISSN 2668-4756
Article DOI: https://doi.org/10.35219/mms.2020.4.06

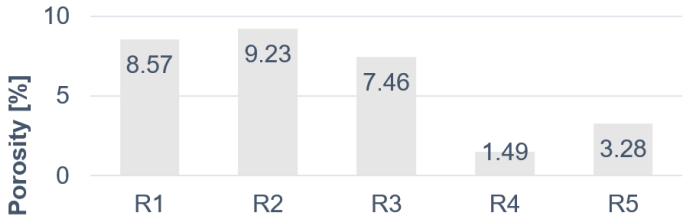

Fig. 6. *Porosity depending on the composition of the porcelain mass fired at a temperature of 1250 ℃*

3.2. Structural analysis of samples

For the study of the structure, the Olympus optical microscope was used both on the pressing surface and in the sample break (Fig. 7-11).

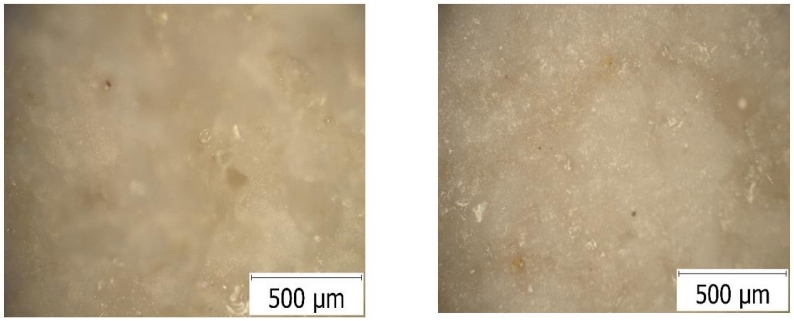

Fig. 7. *Sample structure R1 (Kaolin 25%; Feldspar 20%; Quartz 15%; Bone ash 40%, 25% kaolin). (X100). a - in breaking the sample; b -on the surface of the sample*

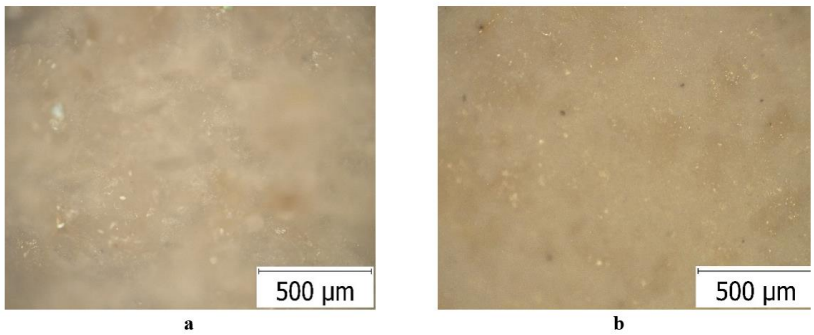

Fig. 8. *Sample structure R2. (Kaolin 25%; Feldspar 13%; Quartz 12%; Bone ash 50%.). (X100). a - in breaking the sample; b -on the surface of the sample*

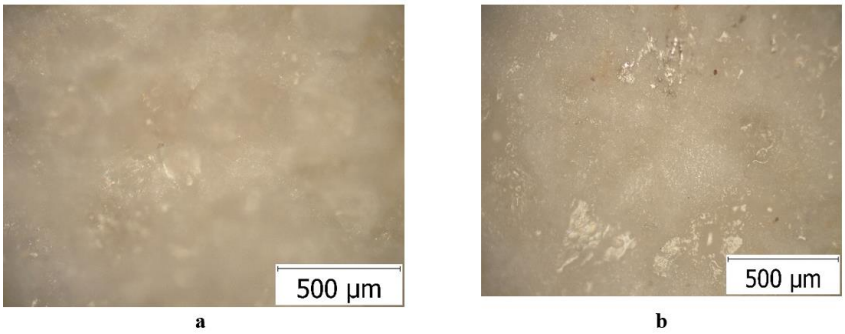

Fig. 9. *Sample structure R3. (Kaolin 20%; Feldspar 15%; Quartz 15%; Bone Ash 50%) (X100). a - in breaking the sample; b -on the surface of the sample*

THE ANNALS OF "DUNAREA DE JOS" UNIVERSITY OF GALATI
FASCICLE IX. METALLURGY AND MATERIALS SCIENCE
N°. 4 - 2020, ISSN 2668-4748; e-ISSN 2668-4756
Article DOI: https://doi.org/10.35219/mms.2020.4.06

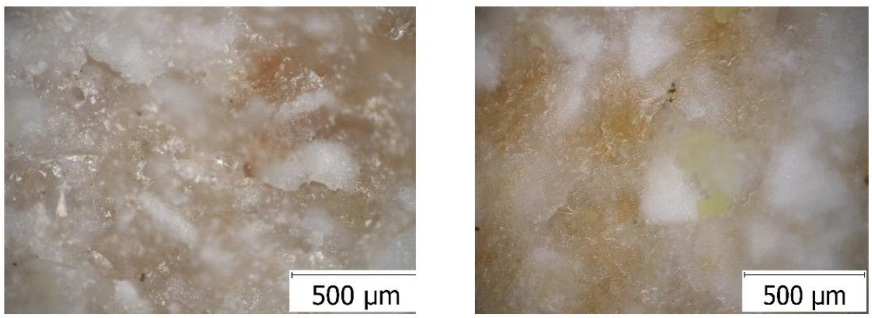

a b

Fig. 10. *Sample structure R4 (Kaolin clay 40%; Feldspar 20%; Bone ash 40%). (X100). a - in breaking the sample; b -on the surface of the sample*

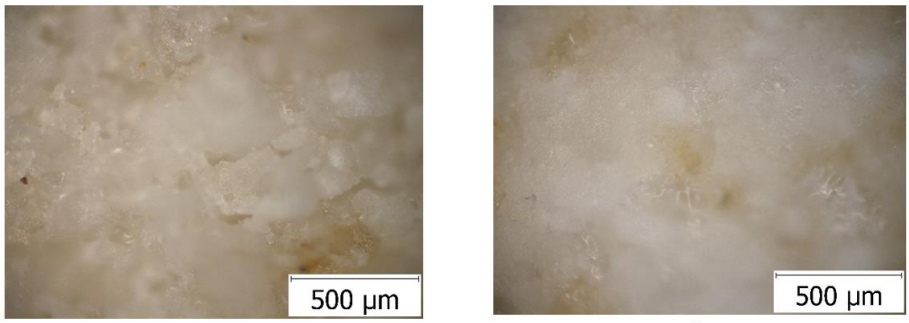

a b

Fig. 11. *Sample structure R5. Kaolin clay 30%; Feldspar 15%; Quartz 5%; Bone ash 50% (X100). a - in the sample crack; b - on the sample surface*

4. Conclusions

The structural aspect studied under the light microscope indicates that in all samples the process of porcelain formation was initiated by the appearance of the glass phase, which partially dissolves the clay substance containing Al_2O_3 as well as calcium oxide and phosphorus pentoxide which resulted from the decomposition of phosphate. calcium from bone ash.

Of all the compositions tested, the one marked with R4, which contains kaolin clay instead of kaolin and does not contain quartz, has densified the most with an open and intercommunicating porosity of 1.49% compared to the maximum porosity obtained in sample R2 of 9.23%. This can be explained by the fact that the kaolin clay used contained free silicon dioxide with micrometric particles and a lower proportion of Al_2O_3 than kaolin, which led to the formation of the vitreous phase in a shorter time.

References

[1]. ***, http://lucia.neagu.com/20180723/lumea-ceramicii/.
[2]. ***, https://www.scribd.com/doc/55666092/Evolutia-Ceramicii.
[3]. ***, Dalea I., O istorie a artei ceramice, Editura Meridiane 1987.
[4]. Suter C., *Istoria Artei Plastice*, vol. 1, Editura Didactica și Pedagogica, Bucuresti.
[5]. Slatineanu B., *Ceramica Romaneasca*, Studii de arta, Editura de stat, 1958.
[6]. Marincas L., *Procedee de fabricare în industria ceramicii*, 2006.
[7]. Baltă P., Tehnologia sticlei, Editura tehnică, 1984.
[8]. Patrick Naylor W., *Introduction to Metal-Ceramic Technology*, Third Edition, 2017.
[9]. Cai Z., Bunce N., Nunn M. E., Okabe T., *Porcelain adherence to dental cast CP titanium: effects of surface modifications*, Biomaterials, 22 (9), 979-86, 2001 May.
[10]. Hench L. L., Bioceramics J. Am. Cer. Soc., 81 (7), p. 1705-1728, 1998.
[11]. Hench L. L., Wilson J., *An Introduction to Bioceramics, Advanced Series in Ceramics*, vol. 1, World Scientific Publishing, 1993.
[12]. Craig R. G., *Restorative Dental Materials*, Mosby, 1997.
[13]. Forna Norina Consuela, *Protetica Dentara*, Editura Univers Enciclopedic, Bucuresti, 2011.
[14]. ***, https://ro.wikipedia.org/wiki/Por%C8%9Belan.

THE ANNALS OF "DUNAREA DE JOS" UNIVERSITY OF GALATI
FASCICLE IX. METALLURGY AND MATERIALS SCIENCE
N°. 4 - 2020, ISSN 2668-4748; e-ISSN 2668-4756
Article DOI: https://doi.org/10.35219/mms.2020.4.07

THE EFFECT OF FLUORIDE CONTAINING TOOTHPASTE ON THE ELECTROCHEMICAL BEHAVIOR OF 316L STAINLESS STEEL FOR DENTISTRY APPLICATIONS IN THE HUMAN SALIVA

Veaceslav NEAGA, Lidia BENEA
Competences Center: Interfaces-Tribocorrosion-Electrochemical Systems
"Dunarea de Jos" University of Galati, Romania
e-mail: lidia.benea@ugal.ro

ABSTRACT

The study aims to investigate the effect of fluorinated toothpaste added in Fusayama-Meyer saliva in order to evaluate the electrochemical behavior of 316L-SS for dentistry applications.

For electrochemical behavior in situ electrochemical measurements such as: Open circuit potential (OCP), Linear Polarization (PL), Potentiodynamic Polarization (PD) and Electrochemical Impedance Spectroscopy (EIS) were applied. The results show a comparative analysis of the electrochemical behavior and corrosion resistance of 316L-SS in human saliva containing high fluoride toothpaste for dentistry applications. From the electrochemical results it can be concluded that the addition of fluoride toothpaste in Fusayama-Meyer saliva decreases the corrosion resistance of 316L-SS and therefore will reduce the lifetime of dentistry structures or devices.

KEYWORDS: orthodontic devices; 316L stainless steel; corrosion; electrochemical methods; saliva; toothpaste

1. Introduction

Stainless steel AISI 300th series of steels has high rates of corrosion resistance, strength and flexibility. They can be used with equal success in the food [1], pharmaceutical industries [2] or dental medicine [3]. However, in recent years, interest in AISI 316L (316L-SS) has increased from economic considerations (low cost, reasonable strength, corrosion resistance and biocompatibility) [4-5]. For example, in dentistry, it is used in a variety of applications (endodontic files in root canal therapy, sterilized instruments, metal posts in root canal treated teeth, arch wires, temporary crowns and brackets in orthodontics) [5]. This can be attributed primarily to corrosion resistance. Moreover, this resistance concerns not only atmospheric phenomena, but also acidic and alkaline media present in the oral cavity of healthy or sick patients.

In the context of the mechanical systems, making orthodontic metallic devices and their subsequent use in the oral cavity for a long time, requires utmost attention to the corrosive process of the material in aggressive environments due to factors such as salivary pH, temperature, quantity of microelements (F, Cl) and enzymatic activity of bacterial micro flora.

Consequences of the corrosive process represented by surface modification and increased roughness cause a decrease in the mechanical strength of the alloys in time [6-7].

Last but not least, the recommendations of the specialists regarding oral hygiene as a preventative treatment of orthodontic treatment should be considered, where dental brushing is the basis of the process of removing food debris and plaque accumulated around orthodontic appliances to counteract the development of dental and periodontal pathologies [8]. Among other things, the latest research demonstrates a better preventative result of diurnal and nocturnal brushing with Fluorine 5000 ppm fluoride toothpaste than the combination of once daily fluoride toothpaste 1000 ppm and rinse with sodium fluoride 500 ppm [9].

However, other studies appreciate the presence of sodium fluoride in products of oral hygiene, as initiator of the corrosive process by the formation of hydrofluoric acid (HF) after reacting of fluorine and hydrogen ions produced by bacteria, with role to destroy the protective oxide layer on the surface

THE ANNALS OF "DUNAREA DE JOS" UNIVERSITY OF GALATI
FASCICLE IX. METALLURGY AND MATERIALS SCIENCE
N°. 4 - 2020, ISSN 2668-4748; e-ISSN 2668-4756
Article DOI: https://doi.org/10.35219/mms.2020.4.07

orthodontic metal components [6, 10-11] or increase friction force [12]. In some recent studies, corrosion mechanisms of stainless steel have been examined in various solutions, including different artificial saliva [5, 13-16].

The purpose of this work is to evaluate the corrosion resistance of AISI 316L stainless steel in terms of their suitability for dentistry applications in two different artificial saliva with Fluoride as 1400 ppm toothpaste and non-fluoride one. Comparative corrosion evaluation was performed using electrochemical techniques as open circuit potential, potentiodynamic measurements and electrochemical impedance spectroscopy measurements at free potential. In the literature there is a lack of information regarding the influence of fluorinated toothpaste on the corrosion behavior of stainless steel in saliva for dentistry applications. This research work aims to investigate the effect of fluorinated toothpaste added to human saliva on the corrosion behavior of 316L stainless steel used in orthodontic applications.

2. Materials and methods

2.1. Materials and methodology

In this experimental study, the samples of AISI 316L stainless steel purchased from Direct Line Inox, Bucharest in a form of sheets with the following dimensions 250 mm x 250 mm and 1.5 mm thickness, with compositions in mass fractions as shown in Table 1.

Table 1. *Chemical composition in mass percent of the AISI 316L stainless steel*

Chemical compositions (wt%)							
Chemical element	**C**	**Mn**	**Si**	**Mo**	**Ni**	**Cr**	**Fe**
316L SS	≤0.03	≤2	1	2.0-2.5	11-14	16.5-18.5	Bal.

Each group of the samples AISI 316L SS samples were investigated to one of two media: SFM (human Saliva Fusayama-Meyer) [4, 17] and SFM mixed with fluoride-containing toothpaste. The chemical composition of Fusayama Meyer saliva can be seen in Table 2.

Composition of fluorinated toothpaste (ParodontaxR) (1400 ppm F^- ion) describes these components: Sodium Bicarbonate, Aqua, Glycerin, Cocamidopropyl Betaine, Alcohol, Krameria Triandra (Ratanhia), Mentha Piperita Oil, Mentha Arvensis Oil, Echinacea Purpurea, Commiphora Myrrha, Chamomilla Recutita, Salvia Officinalis (Sauge) Oil, Sodium Fluoride, Sodium Benzoate, Xanthan Gum, Sodium Saccharin, Limonene, CI 77491.

This study also involves a method of calculating the physiological proportions of human saliva and fluorinated toothpaste, used in another research field, where it proposes a mixture of paste and solution in a ratio of 1:4 (w/v) [6].

In this experiment it was used a solution of human saliva in volume of 150 mL mixed with 37.5 g fluorinated toothpaste. The reported volume between saliva and toothpaste represents the quantity of oral fluid exposed to a healthy person during a 3-4 minute dental brushing, where the average normal stimulated salivary secretion is 1 mL / minute [18].

Table 2. *Chemical composition of Fusayama-Meyer saliva*

Nr. crt.	**Compound**	**Saliva Fusayama Meyer [g/L]**
1	NaCl	0.4
2	KCl	0.4
3	$CaCl_2$	0.8
4	$NaH_2PO_4*12H_2O$	0.79
5	UREA	1
6	**pH**	**5.7**

The samples used as the working electrodes were cut into 25 x 25 mm plate with 1.5 mm thickness and solder with an electrical cable to have electrical contact and insulated with epoxy resin leaving a working area exposed for electrochemical tests resulted at 225 mm^2 (15 mm x15 mm). The sides and the conductive cable contact area were protected by an inert resin layer. The electrochemical measurements were carried out with three-electrode electrochemical station in a 250 mL cell and managed

THE ANNALS OF "DUNAREA DE JOS" UNIVERSITY OF GALATI
FASCICLE IX. METALLURGY AND MATERIALS SCIENCE
N°. 4 - 2020, ISSN 2668-4748; e-ISSN 2668-4756
Article DOI: https://doi.org/10.35219/mms.2020.4.07

by hardware device VoltaLab PGZ 100 with software controlled VoltaMaster 4 by a personal computer. In the electrochemical cell, the AISI 316L stainless steel work electrode (WE) and the auxiliary electrode (AE) consisting of a Pt-Rh grid were spatially arranged parallel and on the same distances between electrodes. The reference electrode Ag/AgCl with KCl saturated solution (E = +199 mV) is placed halfway between WE and AE [19].

Before each experiment, the AISI 316L stainless steel samples were cleaned with ethanol 99.3% after then rinsed in distilled water and dried. For each experiment it was established a volume of 150 mL solution. All experiments have been conducted at room temperature of 25 °C.

The electrochemical methods were focused on the following corrosion tests: Open circuit potential (OCP) measured for a period of 720 minutes and monitored over time until it reached a stable state value relative to the Ag/AgCl reference electrode (RE).

The linear and potentiodynamic polarization were performed after 28 hours of immersion of the sample and consisted of imposing a potential amplitude of ±50 mV around free potential or imposing a variable potential (range from -1 V to +1.5 V/Ag/AgCl) between the working electrode (WE) and the reference electrode (RE) with a scan rate: 1 mV/s.

Measurements of Electrochemical Impedance Spectroscopy makes it possible, without disturbing the nature of the flow of operation, to study the kinetics and mechanism of corrosion processes, passivation mode and the formation of protective films on metals, as well as the adsorption behavior of inhibitors. Electrochemical Impedance Spectroscopy (EIS) after 12 hours of immersion were performed in a spectrum value from 100 kHz to 1 mHz, where the alternate applied signal has a sine wave amplitude of 10 mV with a frequency per decade of 10 Hz and 0.1 s delay before integration. All recorded EIS measurements were analyzed as Nyquist and Bode diagrams using the ZView 3.4e software for fitting the experimental data. To verify reproducibility, each experiment was repeated four times.

3. Results and discussions

3.1. Open circuit potential (OCP)

The variation of the open circuit potential is used as a criterion for determining the corrosion behavior tendency of a material in an oxidizing environment. OCP measurements of AISI 316L stainless steel immersed in saliva Fusayama Meyer and SFM with fluorinated toothpaste are presented in Figure 1.

The physico-chemical characteristics of prepared solutions used for corrosion investigations were measured with a multi-parameter analysis device CONSORT C-533 were used. The results are displayed in Table 3.

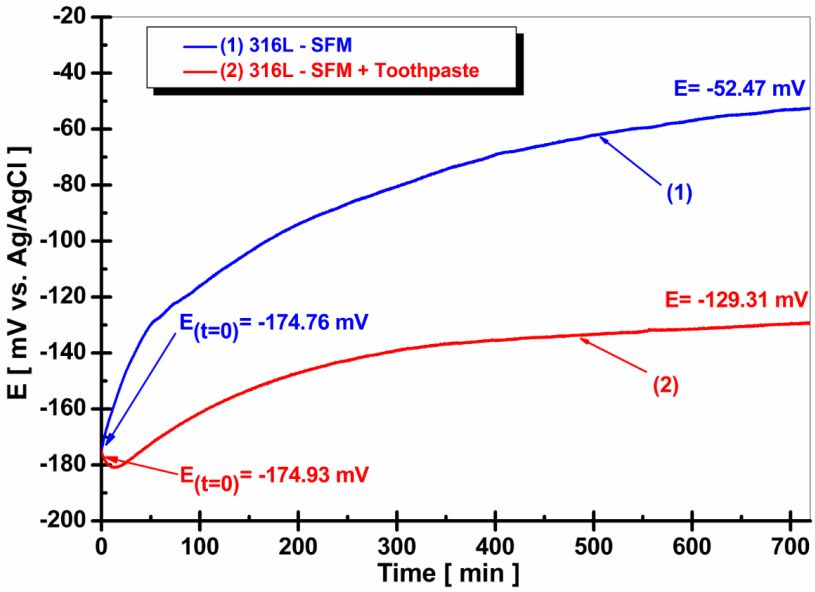

Fig. 1. *Evolution of open circuit potential during 12 hours of immersion of 316L stainless steel in: (1) Saliva Fusayama-Meyer; (2) Saliva Fusayama-Meyer with fluorinated toothpaste*

THE ANNALS OF "DUNAREA DE JOS" UNIVERSITY OF GALATI
FASCICLE IX. METALLURGY AND MATERIALS SCIENCE
N°. 4 - 2020, ISSN 2668-4748; e-ISSN 2668-4756
Article DOI: https://doi.org/10.35219/mms.2020.4.07

Table 3. *Characteristics of Fusayama Meyer saliva*

Simulated Body Fluid	pH	Salinity	Conductivity [mS/cm]
Saliva Fusayama Meyer	5.7	1.3	2.6
Fusayama Meyer + Fluorinated toothpaste	8.1	26.3	42

From Figure 1, the open circuit potential recorded for 12 hours in two different pH solutions (5.7 and 8.1) show that the starting values or the immersion time values of open circuit potential are very close, respectively -174.76 mV vs. Ag/AgCl in SFM with pH 5.7 and -174.93 mV vs. Ag/AgCl in SFM with toothpaste (pH 8.1). The transition tendency to passive potentials in SFM with pH 5.7 is at more positive values reaching a steady state value of -52.47 mV vs. Ag/AgCl. Comparing to the open circuit potential in fluorinated medium with pH 8.1, the passive potential is established to more negative values and the steady state value is reached at -129.31 mV vs. Ag/AgCl at the end of measurement.

In order to determine the influence of the pH factor besides F^- ion, the samples were tested with other electrochemical methods.

3.2. Linear polarization (LP)

From the linear polarization diagram, quantitative information on the polarization resistance and corrosion currents can be extracted from the curve slope according to the Stern- Geary equation [5].

$$i_{cor} = \frac{B}{R_p} \quad (1)$$

While the Stern-Geary parameter B was calculated using equation:

$$B = \frac{b_a|b_c|}{2.303(b_a + |b_c|)} \quad (2)$$

where: icor= corrosion current density; Rp=polarization resistance; ba and bc are the Tafel slopes for anodic and cathodic reactions on linear polarization curves. The increase of polarization resistance means the decrease of corrosion current, therefore the decrease of corrosion rate.

In Figure 2, the linear polarization curves of AISI 316L SS are shown. It is observed that the corrosion potential (Ecor) for stainless steel immersed in Fusayama Meyer saliva mixed with fluorinated toothpaste with pH 8.1 is shifted to more negative value, mV vs. Ag/AgCl as compared with corrosion potential revealed by stainless steel in Fusayama Meyer without toothpaste with pH 5.7, mV vs. Ag/AgCl.

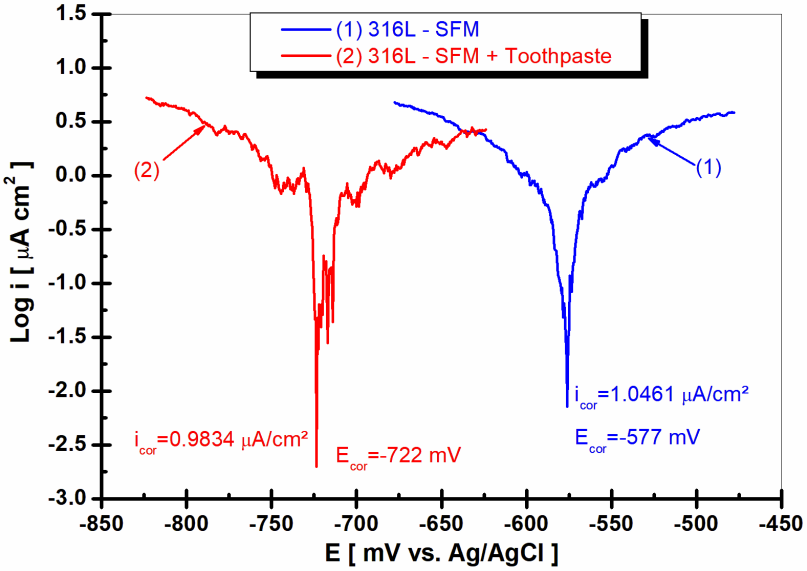

Fig. 2. *Linear polarization diagrams around free potential of 316L stainless steel in: (1) Saliva Fusayama-Meyer; (2) Saliva Fusayama-Meyer with fluorinated toothpaste at a sweep rate of 1 mV/s*

THE ANNALS OF "DUNAREA DE JOS" UNIVERSITY OF GALATI
FASCICLE IX. METALLURGY AND MATERIALS SCIENCE
N°. 4 - 2020, ISSN 2668-4748; e-ISSN 2668-4756
Article DOI: https://doi.org/10.35219/mms.2020.4.07

The corrosion current density reveals about the same values for stainless steel, both values being in the same order of magnitude as it can be seen in Fig. 2.

3.3. Potentiodynamic polarization

Potentiodynamic polarization diagrams were performed in Fusayama Meyer solution with and without fluorinated toothpaste. The results are presented in Figure 3 (a, b). Figure 3a show the entire domain of current density and potential while Figure 3b show a zoom in the range of lower current densities in order to observe better the passive domains of stainless steel immersed in saliva SFM and saliva SFM mixed with toothpaste.

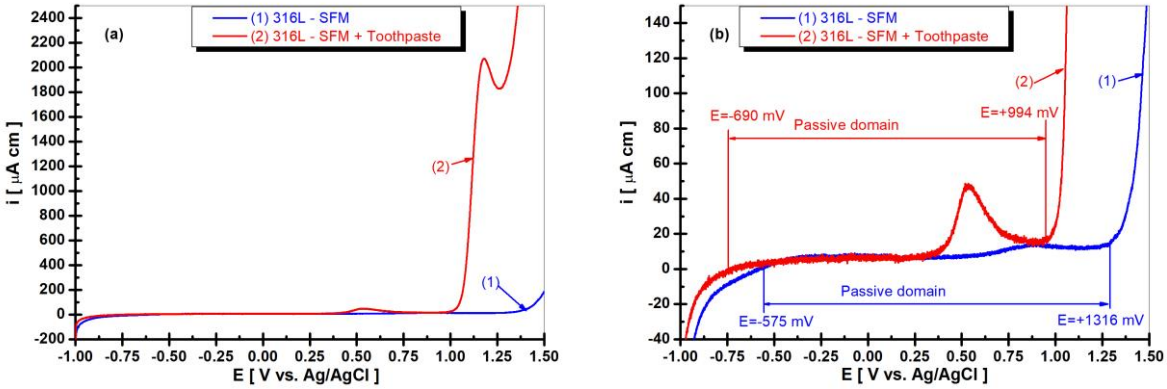

Fig. 3. *Potentiodynamic polarization diagrams of 316L stainless steel performed at a sweep rate of 1 mV/s in: (1) Saliva Fusayama-Meyer; (2) Saliva Fusayama-Meyer with fluorinated toothpaste*

As it is shown in Figure 3a the current density in transpassive domain of stainless steel immersed in saliva mixed with fluorinated toothpaste increases rapidly having higher values as compared with the current density of stainless steel in transpassive domain corresponding to Fusayama Meyer saliva without toothpaste. The passive domain of stainless steel immersed in Fusayama Meyer solution is wider extending over 1316 mV as it can be seen in Figure 3b. When human saliva is mixed with fluorinated toothpaste the passive domain of 316L stainless steel becomes narrower stretching only on 994 mV. It appears also that localized corrosion through passive film occurs when saliva is mixed with fluorinated toothpaste, Figure 3b, diagram (2).

3.4. Electrochemical impedance spectroscopy

In this section, the results obtained by the impedance spectroscopy method complement the open circuit and polarization measurements. To more clearly identify the features of the electrochemical corrosion behavior of AISI 316L stainless steel in human saliva environment with and without addition of fluorinated toothpaste, tests were performed to measure the impedance of an electrochemical cell when a small amplitude sinusoidal voltage is applied to it. As a result of the EIS measurements and its graphical dependence of Z = f (ω), where ω is the angular frequency, in the coordinates of complex ohmic plane, the real component (Re Z) is plotted along the x axis, and the imaginary component of the resistance (- Im Z) is plotted along the y axis [20]. Figure 4 shows the impedance spectrum in the Nyquist graphs, with a higher specific resistance of 316L stainless steel in Fusayama-Meyer saliva, R= 4370 as compared with the specific resistance obtained in human saliva mixed with fluoride toothpaste, R = 1200 kohm·cm^2.

To simulate and fit the EIS experimental results an equivalent electrical circuit model is proposed to express the interface of stainless steel in contact with human saliva. Characterizing the corrosion processes occurring on their surface. The impedance is expressed by the following equation [21-22]:

$$Z_{CPE} = \frac{1}{Q(j\omega)^{\alpha}} \qquad (3)$$

where: Q is the frequency-independent real constant of the CPE in F cm-2 sα-1, ω is the angular frequency ($\omega = 2\pi f$) in rad s¹⁻, f is frequency Hz, j is the imaginary number, $j = \sqrt{-1}$, α is related to the angle of rotation of a purely capacitive line on the complex plane plots.

THE ANNALS OF "DUNAREA DE JOS" UNIVERSITY OF GALATI
FASCICLE IX. METALLURGY AND MATERIALS SCIENCE
Nº. 4 - 2020, ISSN 2668-4748; e-ISSN 2668-4756
Article DOI: https://doi.org/10.35219/mms.2020.4.07

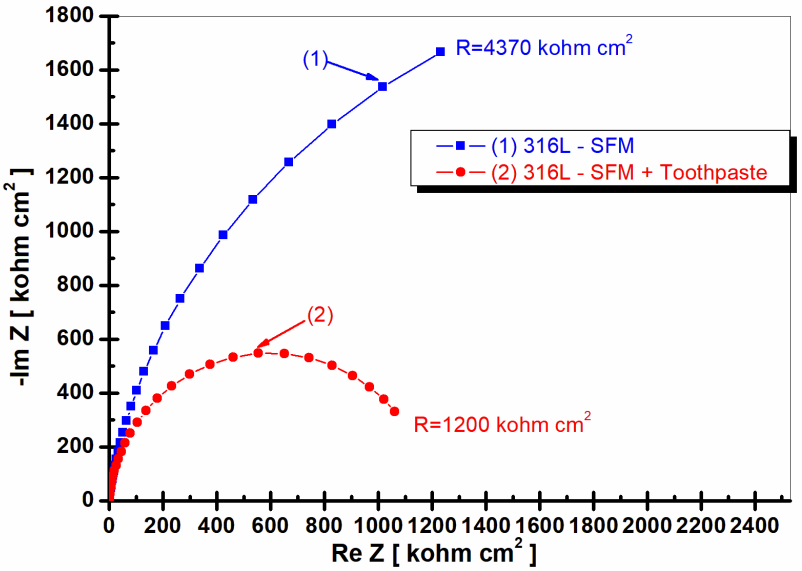

Fig. 4. *Nyquist graphs of the impedance results for the AISI 316L stainless steel immersed in: (1) Saliva Fusayama-Meyer; (2) Saliva Fusayama-Meyer with fluorinated toothpaste*

The time constant dispersion, CPE is attributed to capacity dispersion or to capacity change with frequency. For this research work the constant phase elements (CPE) could express the irregularity of the electrode surface. The value of α is associated to the non-uniform distribution of current as the result of surface inhomogeneity (roughness, structure, defects). The parameter α can takes values from -1 to 1 [23]. In the case when $\alpha \neq 1$, the system reveals a behavior that attributes heterogeneity or the continuously distributed time constants for charge-transfer reactions [5].

The modified Randles circuit with two-time constants, with schematic presentation in Fig. 5, was proposed to fit the EIS experimental results. In this circuit R_s is the solution resistance, CPE_1 is an element of the first constant phase, R_1 is the specific resistance for the first time constant, R_2 is the solution and the corrosion product film resistance and CPE_2 establish the second element constant phase [24]. The first time constant (R_1-CPE_1) is connected with bulk steel passive film interface controlling the dissolution of steel elements and also formation of passive film on stainless steel surface. The second time constant (R_2, CPE_2) describes the passive film/saliva solution interface. This interface controls and at the same time slows down the corrosion degradation process.

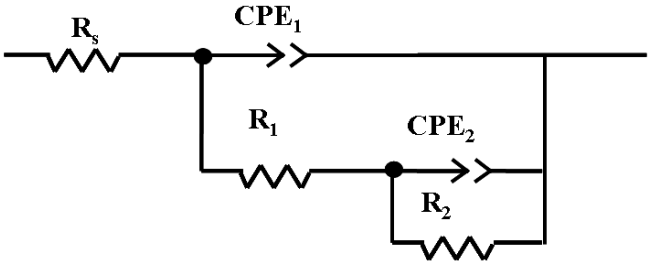

Fig. 5. *The equivalent electrical circuits of AISI 316L stainless steel surface used for better fitting and simulation of electrochemical experimental measurements of the impedance spectra*

The proposed equivalent electrical circuit fits well the Nyquist impedance experimental data but also the Bode plots and admittance plots as module Z versus frequency and phase element versus frequency. The Bode plots, Figure 6 (a) and (b) are displayed an acceptable agreement between experimental and simulated data, thereby validating the selected equivalent circuit model.

THE ANNALS OF "DUNAREA DE JOS" UNIVERSITY OF GALATI
FASCICLE IX. METALLURGY AND MATERIALS SCIENCE
N°. 4 - 2020, ISSN 2668-4748; e-ISSN 2668-4756
Article DOI: https://doi.org/10.35219/mms.2020.4.07

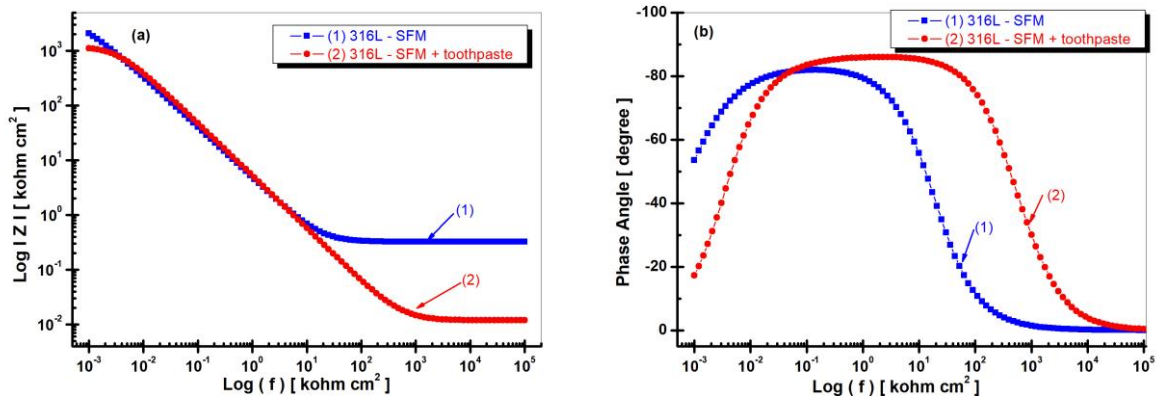

Fig. 6. *Electrochemical Impedance Spectroscopy results (symbols) and fitting diagrams (plain lines) in the Bode coordinates for the AISI 316L stainless steel immersed in: (1) Fusayama Meyers saliva; (2) Fusayama-Meyer saliva mixed with fluorinated toothpaste. (a) - module Z vs. logarithm of frequency and (b) phase angle versus logarithm of frequency*

Table 4 summarizes the values of the circuit parameters obtained from the best fit with the experimental impedance diagrams.

The results obtained after fitting the EIS data using the proposed equivalent circuit (EC), are describing major or minor differences between the two tested solutions. The R values showed on Nyquist impedance data from Figure 4 are values obtained by summing R1 and R2 for respective saliva solution. The R values for SFM solution and for SFM mixed with fluorinated toothpaste are of the same order of magnitude but with slower decrease for 316L stainless steel immersed in Fusayama Meyer saliva mixed with fluorinated toothpaste (about four time smaller) indicating a slower increasing of corrosion rate due to fluor ions containing the toothpaste.

Table 4. *Fitted values for the different elements of the electrical equivalent circuits for the impedance experimental results of 316L stainless steel immersed in Fusayama Meyer saliva with and without fluorinated toothpaste*

Elements of the equivalent circuit	R_1 [kΩ cm^2]	CPE_1 [F cm^{-2}]	R_2 [kΩ cm^2]	CPE_2 [F cm^{-2}]	α	R [kΩ cm^2]
Fusayama-Meyer saliva	129	4.38E-7	4241	3.77E-5	0.92	4370
Fusayama-Meyer saliva + fluorinated toothpaste	72	2.08E-5	1128	1.20E-5	0.88	1200

Tables 4 indicates values of the α element of 0.92 with the tendency towards pure capacitive behavior for stainless steel immersed in Fusayama Meyer saliva. A slower value of α parameter of 0.88 is obtained after fitting the impedance results of 316L stainless steel immersed in Fusayama Meyer saliva mixed with fluorinated toothpaste.

4. Conclusion

The study presents the corrosion behavior of AISI 316L stainless steel in Fusayama Meyer saliva and the effect of fluorinated toothpaste on corrosion resistance. The results of open circuit potential evolution reveal that AISI 316L stainless steel immersed in Fusayama Meyer saliva show a passive state with the tendency to slow increase to more positive values as compared with the evolution of open circuit potential of stainless steel immersed in saliva mixed with toothpaste, which is shifted from the beginning of immersion to more negative values and the steady state value is stated at more negative value also.

Analyzing the linear polarization diagrams it is concluded that the corrosion potential is obtained at more negative value for AISI 316L Stainless Steel immersed in Fusayama Meyer saliva as compared with saliva mixed with fluorinated toothpaste, even if the corrosion current densities reveal the values of same order of magnitude.

The polarization curves in the potentiodynamic regime denoted that the passive domain in the solution without the toothpaste is larger than those revealed in saliva mixed with fluorinated toothpaste.

From the Electrochemical Impedance Spectroscopy can be concluding that AISI 316L SS immersed in artificial Fusayama Meyer saliva have a higher value of specific polarization resistance as compared to human saliva mixed with toothpaste.

Therefore, the recommendations of dentists regarding dental brushing with fluorinated toothpaste for orthodontic patients require a readjustment of the oral hygiene products suggested with those without the fluorinated component.

Acknowledgments

The authors acknowledge the support of this work by the project ANTREPRENORDOC, in the framework of Human Resources Development Operational Programme 2014-2020 (POCU), financed from the European Social Fund under the contract number 36355/23.05.2019 HDR OP/380/6/13 - SMIS Code: 123847.

Disclosure of interest

The authors declare that they have no competing interest.

References

[1]. Dewangan A. K., Patel A. D., Bhadania A. G., *Stainless steel for dairy and food industry: a review*, J Material Sci Eng, 4: 1000191, 2015.

[2]. Ceschini L., Martini C., Rotundo F., *Sliding contacts for the pharmaceutical industry: failure analysis and dry sliding tests for the replacement of hard Cr on AISI 316L steel*, Tribol Int, 81: 248-257, https://doi.org/10.1016/j.triboint.2014.09.004, 2015.

[3]. Asri R. I. M., Harun W. S. W., Samykano M., Lah N. A. C., Ghani S. A. C., Tarlochan F., Raza M. R., *Corrosion and surface modification on biocompatible metals: A review*, Mater Sci Eng C 2017, 77: 1261-1274, https://doi.org/10.1016/j.msec.2017.04.102.

[4]. Holmes D., Sharifi S., Stack M. M., *Tribo-corrosion of steel in artificial saliva*, Tribol Int, 75: 80-86. https://doi.org/10.1016/j.triboint.2014.03.007, 2014.

[5]. Simionescu N., Ravoiu A., Benea L., *Electrochemical in-vitro properties of 316L stainless steel for orthodontic applications*, Rev Chim, 70: 1144-1148, 2019.

[6]. Tipanan Y., Pasutha T., Pintu C., *Corrosion of metal orthodontic brackets and archwires caused by fluoride-containing products: Cytotoxicity, metal ion release and surface roughness*, Orthod Waves, 77: 79-89, 2018.

[7]. Oshida Y., Sellers C. B., Mirza K., Farzin-Nia F., *Corrosion of dental metallic materials by dental treatment agents*, Mater Sci Eng C, 25: 343-348, 2005.

[8]. Anuwongnukroh N., Dechkunakorn S., Kanpiputana R., *Oral hygiene behavior during fixed orthodontic treatment*, Dentistry, 7: 1000457, DOI: 10.4172/2161-1122.1000457, 2017.

[9]. Sudjalim T. R., Woods M. G., Manton D. J., *Prevention of white spot lesions in orthodontic practice: a contemporary review*, Aust Dent J, 51: 284-289. doi: 10.1111/j.1834-7819.2006.tb00445.x, 2006.

[10]. Benyahia H., Ebntouhami M., Forsal I., Zaoui F., Aalloula E., *Corrosion resistance of NiTi in fluoride and acid environments*, Int Orthod, 7: 332-334, doi: 10.1016/S1761-7227(09)73506-5, 2009.

[11]. Kao C. T., Ding S. J., He H., Chou M. Y., Huang T. H., *Cytotoxicity of orthodontic wire corroded in fluoride solution in vitro*, Angle Orthod, 7: 7349-354, 2007.

[12]. Alavi S., Farahi A., *Effect of fluoride on friction between bracket and wire*, Dent Res J, 8: 37-42, 2011.

[13]. Toderascu G., Dumitrascu V., Benea L., Chiriac A., *Corrosion behaviour and biocompatibility of 316 stainless steel as biomaterial in physiological environment*, Fascicle IX. Metallurgy and Materials Science, 4: 16-22, 2015.

[14]. Hayes A., Sharifi S., Stack M. M., *Micro-abrasion-corrosion maps of 316L stainless steel in artificial saliva*, J Bio & Tribo-Corros, 1: 1-25, 2015.

[15]. Jiang R., Wang Y., Wen X., Chen C., Zhao J., *Effect of time on the characteristics of passive film formed on stainless steel*, Appl Surf Sci, 412: 214-222, 2017.

[16]. Benea L., Simionescu N., *Effect of biological solution and pH on corrosion resistance of 304L SS for dental brackets*, Rev Chim, 71: 180-187. https://doi.org/10.37358/RC.20.4.8056, 2020.

[17]. Benea L., Mardare E., Mardare M., Celis J. P., *Preparation of titanium oxide and hydroxyapatite on Ti–6Al–4V alloy surface and electrochemical behavior in bio-simulated fluid solution*, Corros Sci, 80: 331-338, 2014.

[18]. Cheng L., Moor S., Kravchuk O., Meyers I., Ho C., *Bacteria and salivary profile of adolescents with and without cleft lip and/or palate undergoing orthodontic treatment*, Aust Dent J, 52: 315-321, doi: 10.1111/j.1834-7819.2007.tb00508.x, 2007.

[19]. Dumitrascu V. M., Benea L., *Improving the corrosion behavior of 6061 aluminum alloy by controlled anodic formed oxide layer*, Rev Chim, 68: 77-80, 2017.

[20]. Bard A., Faulkner L., *Electrochemical methods. Fundamentals and application*, 2-nd. ed. New York: Wiley, 2001.

[21]. Lasia A., *Modern Aspects of Electrochemistry*, vol 32, ed White RE, Conway BE, Bockris JO'M, New York: Kluwer Academic Plenum Publishers, 1999.

[22]. Brug G. J., Van den Eeden A. L. G., Sluyters-Rehbach M., Sluyters J. H., *The analysis of electrode impedances complicated by the presence of a constant phase element*, J Electroanal Chem Interf Electrochem, 176: 275-295. https://doi.org/10.1016/S0022-0728(84)80324-1, 1984.

[23]. Benea L., Danaila E., Ponthiaux P., *Effect of titania anodic formation and hydroxyapatite electrodeposition on electrochemical behavior of Ti–6Al–4V alloy under fretting conditions for biomedical applications*, Corros Sci, 91: 262-271. https://doi.org/10.1016/j.corsci.2014.11.026, 2015.

[24]. Ribeiro D. V., Souza C. A. C., Abrantes J. C. C., *Electrochemical impedance spectroscopy (EIS) to monitoring the corrosion of reinforced concrete*, Revista IBRACON de Estruturas e Materiais, 8: 529-546, 2015.

THE ANNALS OF "DUNAREA DE JOS" UNIVERSITY OF GALATI
FASCICLE IX. METALLURGY AND MATERIALS SCIENCE
Nº. 4 - 2020, ISSN 2668-4748; e-ISSN 2668-4756
Article DOI: https://doi.org/10.35219/mms.2020.4.08

STUDY ON EXPERIMENTAL DETERMINATION OF THE ELASTICITY MODULUS OF CASTED BASALT

Ilie Octavian POPP
"Lucian Blaga" University of Sibiu, Romania
e-mail: ilie.popp@ulbsibiu.ro

ABSTRACT

Basalt is a material available in big quantities in nature. It has a low price and can be used in various domains. It can be relatively easily extracted from natural deposits and processed by means of melting. Melted and recrystallized basalt has demonstrated promising behavior with regards of its use in manufacturing, as reported in the literature.

This paper presents the results of an experimental study on the determination of the modulus of elasticity of molten and recrystallized basalt by the method of resistive electrical tensometry and to validate the result and by simulation using finite elements method. Testing methodology, experimental test, data records, data processing and resulting conclusions are presented in the paper.

KEYWORDS: materials, experimental study, modulus of elasticity of basalt

1. Introduction

One of the major issues of the contemporary world, in the context of the global crisis of raw materials and materials, is the saving of ferrous and non-ferrous metal, as well as of other deficient and expensive materials. Within this action, the concerns for introducing and extending the use of basalt, a material found in large quantities in nature, accessible and inexpensive are also included. Basalt is the most widespread material on the surface of the earth. It appears in all four major tectonic environments.

Basalt is a natural, hard, dense, dark brown to black volcanic rock originating at a depth of hundreds of kilometers beneath the earth and reaching the surface as molten magma. The simplicity of the manufacturing process reduces the production cost of basalt parts and fibers in industry. The quality and chemical composition of the basalt raw material have a major effect on the costs and properties of the parts and fibers made from this material and can lead broad range of application in industry, with different mechanical properties [1].

From the study of the scientific literature and other researches in the field, the following aspects can be remarks:

Known technologies allow the processing of basalt by [2, 3]:

- melting and recrystallization;
- sintering;
- basalt fibers.

By melting and recrystallization, the basalt improves its main chemical, physical and mechanical characteristics, of which we mention:

- exceptional abrasion resistance, which in most cases exceeds that of high alloy steels;
- very high resistance against acids (sulfuric acid, hydrochloric acid, other strong acids, except for hydrofluoric acid); stability to solutions of sodium hydroxide, potassium hydroxide and other bases;
- special dielectric properties;
- wear resistance by sliding;
- thermal and sound insulation (in the form of wool);
- successfully replaces high alloy steels and castings in the construction of some plants and machinery.

In addition to the advantages presented above, there are still several disadvantages:

- it has no plasticity;
- it doesn't withstand mechanical shocks very well;
- it doesn't resist to thermal shocks, the maximum temperature coefficient of resistance is 400-600 ºC.

The use of basalt products is justified and it is necessary to look for other areas and methods where there could be the possibility of using this material. Although basalt is a material known to specialists in the silicate industry and the construction industry, the

THE ANNALS OF "DUNAREA DE JOS" UNIVERSITY OF GALATI
FASCICLE IX. METALLURGY AND MATERIALS SCIENCE
Nº. 4 - 2020, ISSN 2668-4748; e-ISSN 2668-4756
Article DOI: https://doi.org/10.35219/mms.2020.4.08

same cannot be said about its use in the field of machine construction. The car construction industry has completely different characteristics than the ones found in constructions and that is why extensive research is required in order to highlight the characteristics of basalt, to exploit the advantages offered by it and to eliminate the disadvantages [4].

Therefore, the problem of basalt behavior to specific requests, in order to use it in the manufacture of the structural elements of the machines and equipments has not yet been addressed so this paper aims to make a necessary introduction in this direction. As a result, the elastic modulus and strength of basalt composites as material for machine parts must be evaluated carefully [5, 6].

2. General topics

In machine tool and equipment manufacturing industry, it is necessary to be chosen materials that withstand the demands that may arise in operation. For this, in first phase of design and calculation of dimensioning the structural elements, it is important to know the elastic characteristics of the materials.

Knowing the specific deformations of the material produced during a mechanical stress (axial, bending or twisting) in the elastic field and using the relationships of STAS 10290-86 (Metal testing. Tensile testing. Determination of the elastic characteristics [7]) the numerical values of the elasticity modules E and G can be determined. In addition, with the help of specific deformations the value of the cross-sectional contraction coefficient ν is determined.

For this determination, the method of resistive electrical tensometry was used and the experiments were carried out in the Materials Resistance laboratory of Engineering Faculty of Sibiu. The planning and conduct of these experimental researches were done in compliance with the current standards. Also, the methods of collecting and statistical processing of the experimental data are those recommended by the Romanian standards.

3. Determination of the basalt elastic characteristics by the method of resistive electrical tensometry

Resistive electrical tensometry is a method that allows measuring the specific deformations of the requested part with high precision. In order to determine the coefficient of transverse contraction on a normal flat specimen, two resistive electrical transducers are marked on the opposite sides: one along the axis and the other perpendicular or one rosette with two perpendicular translators. The electric transducers are connected in full deck using the bridge property to algebraically gather the variations of resistors of the transducers connected in the same arm or opposite arms and to algebraically decrease the variations of the resistances of the transducers connected in adjacent arms. The complete bridge assembly avoids the parasitic effects, the translator placed transversely on the specimen having the role of the compensation translator. Transducers with the same value for the voltage constant and the same value for the electrical resistance are chosen. The difference between the indication of the tensometric bridge circuit after loading the specimen and the indication of the bridge before loading the specimen represents the specific deformation read at the strain gauge bridge circuit.

The static constants of elasticity were determined on a number of 16 basalt specimens, of dimensions lxbxh = 16.6 x 11.7 x 240 mm, on which four strain gauges TER1-TER4 linear type SGD-6/120-LY13 were placed, (Fig. 1). The specimens were loaded for simple bending with forces having different numerical values (Table 1) and the tensometric bridge indications representing the specific deformations (ε) were read.

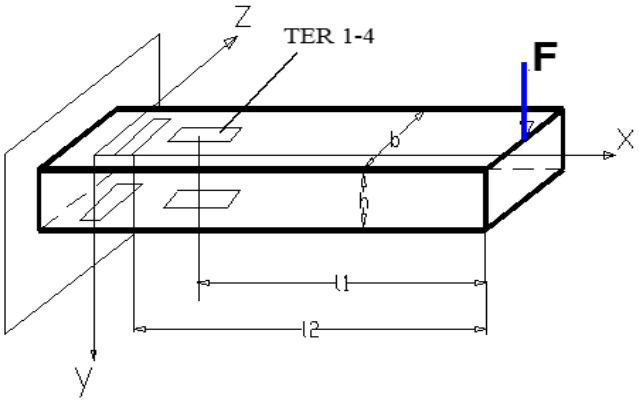

Fig. 1. *The model of the basalt specimen*

THE ANNALS OF "DUNAREA DE JOS" UNIVERSITY OF GALATI
FASCICLE IX. METALLURGY AND MATERIALS SCIENCE
N°. 4 - 2020, ISSN 2668-4748; e-ISSN 2668-4756
Article DOI: https://doi.org/10.35219/mms.2020.4.08

The modulus of static longitudinal elasticity is determined by the relation [7]:

$$E = \frac{6l_1F}{bh^2\varepsilon_{x(z)}} \text{ [N/m}^2\text{]} \quad (1)$$

and the coefficient of the transverse contraction with the relation:

$$\nu = -\frac{\varepsilon_z}{\varepsilon_x} * \frac{l_1}{l_2} \quad (2)$$

where l_1, l_2, b, h are the dimensions of the specimen and have the meaning in Fig. 1, F is the applied force, and ε_x and ε_z are the strain in the x and z directions, expressed in μm/m on the scale of the measuring apparatus.

The transverse elasticity modulus determined statically, considering the molten basalt and recrystallized as an isotropic material, it is calculated with the relation:

$$G = \frac{E}{2(1+\nu)} \text{ [N/m}^2\text{]} \quad (3)$$

The mean values obtained from experimental measurements performed on the casted basalt parts are shown in Table 1.

Table 1. *The numerical values of the test*

F [N]	10	20	25	30
ε_{x1} [μm/m]	+27	+58	+72	+102
ε_{x2} [μm/m]	-30	-58	-82	-102
ε_{z3} [μm/m]	-11	-20	-32	-29
ε_{z4} [μm/m]	+11	+19	+27	+29
E_1 [10^{10} N/m^2]	9.530	8.872	8.652	8.046
E_2 [10^{10} N/m^2]	8.577	8.872	8.597	8.046
E_{med} [10^{10} N/m^2]	9.053	8.872	8.124	8.046
ν'	0.354	0.327	0.386	0.247
ν"	0.318	0.327	0.286	0.247
ν_{med}	0.336	0.327	0.336	0.247
$E = (8.523 \pm 0.512)\ 10^{10}$ N/m^2 $\nu = 0.333 \pm 0.0052$ $G = (3.196 \pm 0.254)\ 10^{10}$ N/m^2				

The experimental data obtained from the tests was analyzed using Microsoft EXCEL. Statistical processing of the measurement results (the values of deformations) was done considering a significance threshold α = 0.05. The Cochran test was applied to determine the homogeneity of the dispersion and the Student test to eliminate the insignificant effects. Interpreting the data obtained from the measurements and using the relationships (1), (2) and (3), the values of the static elasticity modulus E, the coefficient of the transverse contraction ν and the transverse elasticity modulus G, were determined as presented in Table 1.

Behavior tendency of basalt, determined by the series of experimental data presented, was highlighted using Microsoft EXCEL software, through the linear regression method. It draws a line through a series of values resulting from measurements using the least squares method. The linear regression equation (y = ax + b) and the value of R2 are calculated automatically by the program and are displayed in the diagram from Fig. 2.

The experimental values obtained for the elastic constants of the basalt (E, ν, G - Table 1) are useful in knowing the most accurate behavior as a base material or a substitute material in different mechanical constructions. We observe an almost

THE ANNALS OF "DUNAREA DE JOS" UNIVERSITY OF GALATI
FASCICLE IX. METALLURGY AND MATERIALS SCIENCE
N°. 4 - 2020, ISSN 2668-4748; e-ISSN 2668-4756
Article DOI: https://doi.org/10.35219/mms.2020.4.08

linear behavior of the basalt in the analyzed elastic range (Fig. 2). The dispersion obtained is due to the inhomogeneous of the material structure from different batches and due to measurement errors.

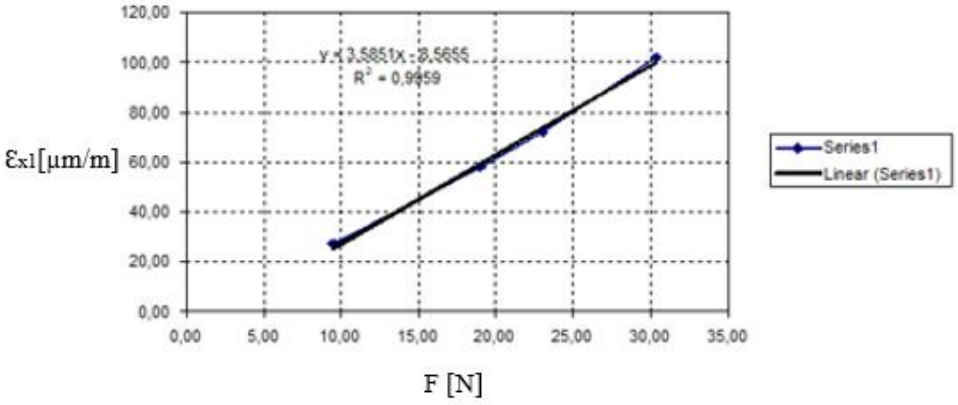

Fig. 2. *Behavior tendency of basalt given by experimental results*

4. FEM of determined elasticity modulus

In order to further validate the experimental data obtained from the tested parts, numerical investigation was performed and a basalt bar was modeled. The simulation of the test was performed through finite element method with the help of Abaqus software package. The analysis of the process followed an implicit scheme in order to obtain results as precise as possible. The basalt part is meshed with the help of C3D8R element with the dimension of 2 mm, thus obtaining 5760 elements on this specimen. The specimen is fixed at one end and on the other forces are applied in the form of 4 pressures in different steps like in Fig. 3a. For the analysis to be carried out the basalt specimen was modeled using the elasticity modulus determined experimentally and Poisson coefficient which was calculated as 0.333.

After running the analysis, when applying the forces of 10 N, 20 N, 25 N and 30 N, the maximum displacement values and the maximum von Mises stresses, presented in Fig. 4 are obtained.

Fig. 3. *Basalt specimen modeled in Abaqus*

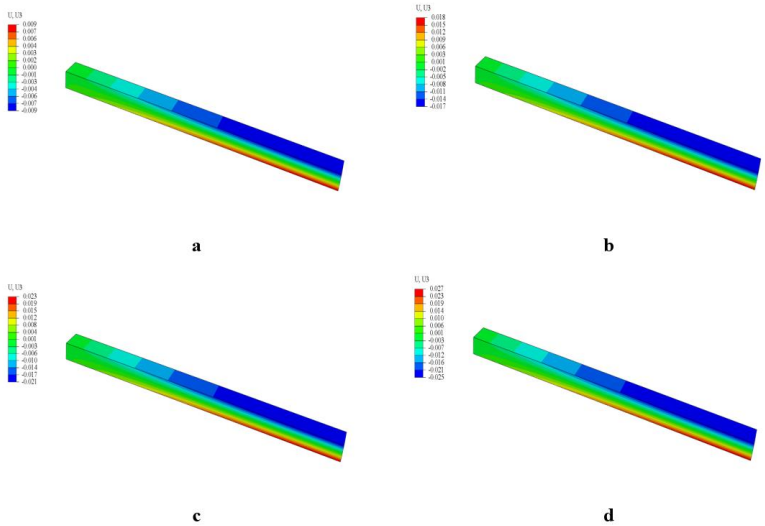

Fig. 4. *Displacement of U3 (axial direction) when a force of 10 N, 20 N, 25 N and 30 N is applied*

THE ANNALS OF "DUNAREA DE JOS" UNIVERSITY OF GALATI
FASCICLE IX. METALLURGY AND MATERIALS SCIENCE
Nº. 4 - 2020, ISSN 2668-4748; e-ISSN 2668-4756
Article DOI: https://doi.org/10.35219/mms.2020.4.08

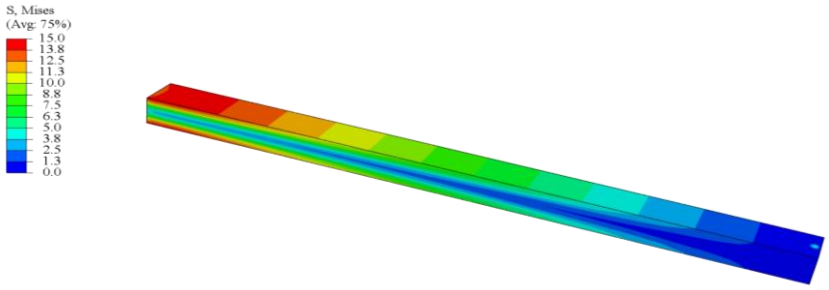

Fig. 5. *The von Mises stresses when a force of 30 N is applied*

A comparison of the values obtained experimentally and through finite element analysis can be seen in Table 2.

Table 2. *Comparison between the values of displacement on axial direction obtained experimentally and through numerical analysis*

Forces [N]	**Displacements obtained experimentally [µm]**	**Displacements obtained through FEM [µm]**
10	6	9
20	14	18
25	17	23
30	24	27

5. Conclusions

The elastic deformations of the loaded elements of machine tools (mullion, sleepers, tines, tables, housings, etc.) must be appreciated in terms of their influence on the precision of the manufacturing of the workpiece. The deformations result from the action of the cutting forces, the own weight of the loaded elements, the weight of the semi-finished product, the clamping forces and sometimes even the forces of moving inertial masses.

The value of the static elasticity modulus of the casted basalt was determined, with the help of bar-type samples subjected to bending through resistive electrical tensometry method. These values obtained from the presented experiments, were taken into account as material characteristics, when modeling the static behavior of the basalt through the method of the finite elements.

Table 2 shows that the values of displacements of the basalt specimen determined through finite element analysis method are approximately with the values obtained experimentally and this is due to the fact that in numerical investigation software, Abaqus, the elasticity modulus E was taken $8.523x10^{10}$ [N/m^2].

References

[1]. Möhring H.-C., Brecher C., Abele E., Fleischer J., Bleicher F., *Materials in machine tool structures*, CIRP Annals - Manufacturing Technology, 64 (2), p. 725-748, 2015.
[2]. Gornic C., *Bazaltul materie primã pentru piesele destinate masinilor unelte*, ICSITMU - Titan Bucuresti, 1989.
[3]. Ducatti V., Lintz R., Santos J., *Comparative Study with Alternative Materials for Manufacture of Machine Tool Structure*, International RILEM Conference on the Use of Recycled Materials in Building and Structures, p. 925-934, 2004.
[4]. Kepczak N., Pawlowski W., *Application of Mineral Casting for Machine Tools Beds*, Mechanics and Mechanical Engineering, 17(4), p. 285-289, 2013.
[5]. Popp I. O., *Consideration regarding the properties and behaviour of basalt used in machine building*, in Proceedings, p. 127-130, First international Conference on Materials and Manufacturing Tehnologies, MATEHN' 94, Cluj-Napoca, 1994.
[6]. Popp I. O., *Contributii la cercetarea comportarii bazaltului supus unor solicitari specifice masinilor unelte*, Teza de doctorat, "Lucian Blaga" University of Sibiu, 1999.
[7]. Mocanu D. R., *et al.*, *Incercarile materialelor*, vol. I, II, Editura Tehnica, Bucureşti, 1982.

THE ANNALS OF "DUNAREA DE JOS" UNIVERSITY OF GALATI
FASCICLE IX. METALLURGY AND MATERIALS SCIENCE
N°. 4 - 2020, ISSN 2668-4748; e-ISSN 2668-4756
Article DOI: https://doi.org/10.35219/mms.2020.4.09

REAL-TIME RAINDROP DETECTION BASED ON DEEP LEARNING ALGORITHM

Florin Bogdan MARIN, Mihaela MARIN
"Dunarea de Jos" University of Galati, Romania
e-mail: florin.marin@ugal.ro

ABSTRACT

The goal of this research is to develop an in-vehicle computerized system able to detect the raindrops on windshield and warn the driver and start the windscreen wiper in order to avoid that computer vision to acquire blurred images. This feature is important in order to develop Advanced Driver Assistance System based on computer vision. The system should be able specific scenarios that do not allow the ADAS computer vision feature to work properly. Rain drop detection will allow a more reliable Advanced Driver Assistance System.

KEYWORDS: computer vision, passenger fatigue detection, Advanced Driver Assistance System

1. Introduction

With more than 50 000 casualties in Europe, Advanced Aided Driver Assistance (ADAS) systems solutions are rapidly becoming an essential feature of many car manufacturer in order to provide road safety. Besides many sensors used (lidar, radar, ultrasonic) computer vision is used mainly in most of ADAS systems such as obstacle detection, lane detection, pedestrian detection. Due to the variable environmental that cameras used in ADAS computer vision application must be used the developer must address additional challenges, such as corrupted data flow or failure of image acquisition. One of the issues is rain-drop detection. In this case, the system automatically starts windshield wipers and/or alert the driver that the system cannot be trusted due to the bad image. There are many attempts to detect weather conditions from videos or images for computer vision applications [1, 5, 6]. Raindrops can be described as transparent sphere reflecting light in a specific pattern to the camera. Also, the light is refracted to the camera leading to a distorting image and build a blurred image. Due to these facts the detection of raindrops can be detected.

Several solutions that are assisting the driver are commercially available or developed as proof of concept [2-4]. Dozens of ADAS features are taking into account traffic sign recognition, forward collision warning, lane warning departure, parking assistance, etc.

Self-driving vehicles, also named autonomous vehicles must also use computer vision processing besides several sensors in order to understand the environment to safely navigate without driver decisions. Consequently, autonomous vehicle needs to detect rain drops detections in order to take actions such as control de windscreen wiper or to inform the driver cannot longer operate in safety.

Real time raindrop detection is significant not only to the ADAS system but also for future autonomous vehicles. The development of such detection techniques is of paramount significance with respect to its contribution in the field of computer vision-based applications applied to ADAS. It is also important to be utilized by all computer vision based ADAS for keeping their feature reliable and ensure the windshield is clear and allows reliable images to be processed. The study will also be significant also for other real time surveillance applications such as security cameras, wild animal surveillance. The detection of raindrop will allow the system to inform the user or to activate windshield wiper [3, 5-7]. The detection of windshield wiper is also another objective for ADAS based computer vision systems, as it shouldn't process information when the wipers are in the scene.

Raindrops on windshields are within large range of shape and size. Due to the fact that position in space is quite short distance to the camera this translates in optic effect such as blur, bad focus of the cameras.

There are several approaches for raindrop detection such as Gaussians filter to detect snow and

THE ANNALS OF "DUNAREA DE JOS" UNIVERSITY OF GALATI
FASCICLE IX. METALLURGY AND MATERIALS SCIENCE
Nº. 4 - 2020, ISSN 2668-4748; e-ISSN 2668-4756
Article DOI: https://doi.org/10.35219/mms.2020.4.09

fog based on the dynamics of the spatial and temporal dimensions of images. This method is detecting in fact texture of the rain drops.

Computer vision programmers also imagined Canny Edge detection algorithm for detection of raindrops. Estimating the amount of raindrops is important in order to asses time to control the windshield wiper, taking into account the visibility.

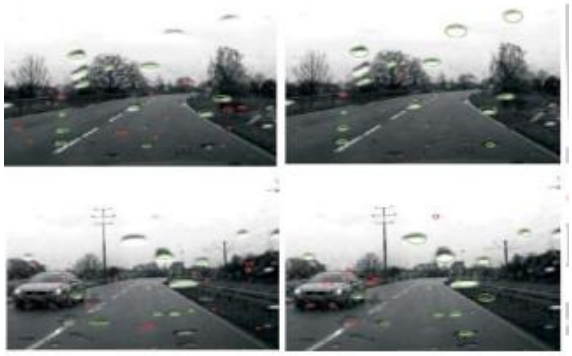

a. BLUR b. RIGSEC+BLUR

Fig. 1. *Detection using BLUR and combination BLUR+RIGSEC. Red marks show False Positives* [1]

Several approaches require settings for as camera optics but this method can only be applied in specific manufacturer hardware and not to the mobile phone application designed as ADAS platform.

Analyzing urban scene images while the sky has the same color as raindrops is a difficult task taking into account that the process must be performed real time and provide fast solutions concerning image registration. It seems that in these areas, the detection rate is low.

The important feature of the deep neural networks is that object detection is based on training the model using several images. In such a way the networks allow learning automatically from training data samples. A deep neural network [4] is I different from a classical neuronal network as it has at least one hidden middle layer (Fig. 2), besides inputs and output layers compared to a classical neural network that have an input and output layer. Each neuronal node forwards a weighted input which is calculated from previous layer. Deep neuronal network is a good solution for many computer vision applications. Light refraction of the raindrops causes color changes depending on the background color.

2. Technique proposed

Experimental results were achieved using a hardware platform made of webcam the Logitech C170 placed on dashboard (Fig. 2), and as processing unit the Lenovo with an Intel® Core™ i5-1035G1 processor. The video sequences were acquired at 20 frames per second. The proposed approach was implemented in Microsoft Visual C++ and OPenCV and OPEN VINO libraries. Figure 2 shows general algorithm to detect drop rain. While preliminary tests have shown that the proposed approach works well in the all-weather environments, during test an accident occurred, the windshield was broken. This might occur at a smaller scale and is leading that ADAS computer vision-based features to fail. In this case the system should warn the driver that ADAS features are not reliable.

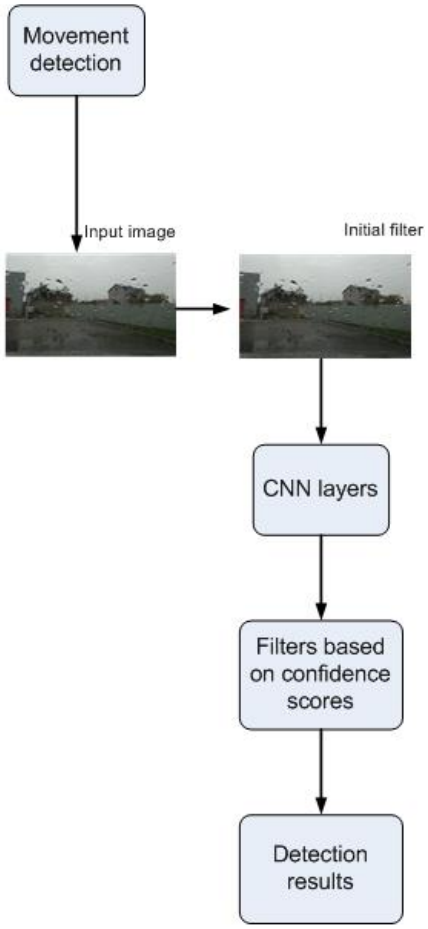

Fig. 2. *General algorithm used for raindrop detection*

A model able of detecting realistic rain drop on glass surfaces demands small amount of dimensional parameterization in order to allow very low computational resources. The algorithm to identify rain (Fig. 3) drop is should run while others computer vision for ADAS are also working, same that might need complex calculations which result in serious computational cost. Moreover, running on the same

THE ANNALS OF "DUNAREA DE JOS" UNIVERSITY OF GALATI
FASCICLE IX. METALLURGY AND MATERIALS SCIENCE
Nº. 4 - 2020, ISSN 2668-4748; e-ISSN 2668-4756
Article DOI: https://doi.org/10.35219/mms.2020.4.09

processing unit of several algorithm to detect lane, obstacles, pedestrians, etc. will make the issue of computational resources important. The neuronal model should run not every frame, but also when the luminosity is changed to a low level, as most raindrop occurred when low luminosity occur, but also there are exceptions concerning weather conditions. In this respect the design parameters should be carefully tuned. CNNs are very efficient because they reuse a lot of weights transmitted across the network. OpenVino was used with Keras learning data in order to train with our data samples. The generic algorithm is described in Fig. 3. The movement detection filters images where motion is detected to some areas, whereas some areas are static. In such a way not all the images are processed in order to achieve a fast overall algorithm, taking into account that this rain drop detection is an auxiliary feature and not the main feature of a ADAS system. The input image is filtered in order to contrast contours with blurred image. The algorithm is tuned in such a way that in case of more than 20% of covering the windshield the system should run the windshield wipers. This percent should be at driver choice in order to achieve best comfort. CNN layers will identify several layers and will provide confidence score that is providing the detection results.

Fig. 3. *Broken windshield*

In case of the accident happened of broken windshield (Fig. 3), the system detected successfully that the image is not accurate in order to be processed. The developed algorithm is detecting most of the raindrops (Fig. 4).

Fig. 4. *Face detection and eye opened detection*

Tested on 10 hours of videos, the algorithm shows a good performance with a rate of detection of 85% of the raindrops on the windshield. Due to the colors similarity we also counted 7% false positive detection (see Tab. 1).

Real-time performance on the processor mentioned indicate a fast algorithm, a frame (1200X800) is processed in 100-200 ms depending on the image and raindrop coverage.

Tab 1. *Statistics concerning feature detected*

No of video sequences	total 10h
Rate of detection	85%
False positive	7%

4. Conclusions

The present study has shown the importance for ADAS system of the feature to detect raindrops in order to run the windshield wiper or to warn the driver. Although the method shows good potential in detecting raindrops from daytime images, given the fact that we use web camera and not night camera, the proposed method is limited to raindrops detection in constraint conditions such as daytime and requires further development to detect raindrops during the night.

References

[1]. Saba N. Karbhari, Pansambal B. H., *Raindrop Detection: Performance analysis of recent approaches for the use in electronic driver assistance systems*.

[2]. Shladover S. E., *Review of the state of development of advanced vehicle control systems*, Vehicle System Dynamics, 24(6–7), p. 551-595, 1995.

[3]. Aurelien Cord, Nicolas Gimonet, *Detecting Unfocused Raindrops: In-Vehicle Multipurpose Cameras*, Robotics & Automation Magazine IEEE, vol. 21, no. 1, p. 49-56, 2014.

[4]. Jonathan Masci, *Advances in Deep Learning for Vision, with Applications to Industrial Inspection Classification, Segmentation and Morphological extensions*, Doctoral Dissertation submitted to the Faculty of Informatics of the Università della Svizzera Italiana.

[5]. Roser M., Geiger A., *Video-based raindrop detection for improved image registration*, in Proc. IEEE Int. Conf. Computer Vision Workshops, p. 570-577, 2009.

[6]. Jee Hun Park, Man Ho Kim, Hong Jun Im, Kyung Chang Lee and Suk Lee, *Development of Vision-Based Control Smart Windshield Wiper System for Intelligent Vehicle*, SICE-ICASE International Joint Conference, 2006.

[7]. Fawazi Nashashibi, Raoul De Charette de La Contrie, Alexandre Lia, *Detection of Unfocused Raindrops on a Windscreen using Low-Level Image Processing*, International Conference on Control, Automation, Robotics and Vision: ICARV, Dec 2010.

MANUSCRISELE, CĂRŢILE ŞI REVISTELE PENTRU SCHIMB, PRECUM ŞI ORICE CORESPONDENŢE SE VOR TRIMITE PE ADRESA:

MANUSCRIPTS, REVIEWS AND BOOKS FOR EXCHANGE COOPERATION, AS WELL AS ANY CORRESPONDANCE WILL BE MAILED TO:

LES MANUSCRIPTS, LES REVUES ET LES LIVRES POUR L'ECHANGE, TOUT AUSSI QUE LA CORRESPONDANCE SERONT ENVOYES A L'ADRESSE:

MANUSCKRIPTEN, ZIETSCHRITFTEN UND BUCHER FUR AUSTAUCH SOWIE DIE KORRESPONDENZ SID AN FOLGENDE ANSCHRIFT ZU SEDEN:

After the latest evaluation of the journals by the National Center for Science Policy and Scientometrics (**CENAPOSS**), in recognition of its quality and impact at national level, the journal will be included in the B^+ category, 215 code (http://cncsis.gov.ro/userfiles/file/CENAPOSS/Bplus_2011.pdf).

The journal is already indexed in:

DOAJ: https://doaj.org/

SCIPIO-RO: http://www.scipio.ro/web/182206

EBSCO: http://www.ebscohost.com/titleLists/a9h-journals.pdf

Google Academic: https://scholar.google.ro

Index Copernicus: https://journals.indexcopernicus.com

Crossref: https://search.crossref.org/

The papers published in this journal can be viewed on the website: http://www.gup.ugal.ro/ugaljournals/index.php/mms

Name and Address of Publisher:
Contact person: Elena MEREUȚĂ
Galati University Press - GUP
47 Domneasca St., 800008 - Galati, Romania
Phone: +40 336 130139
Fax: +40 236 461353
Email: gup@ugal.ro

Name and Address of Editor:
Prof. Dr. Eng. Marian BORDEI
"Dunarea de Jos" University of Galati, Faculty of Engineering
111 Domneasca St., 800201 - Galati, Romania
Phone: +40 336 130208
Phone/Fax: +40 336 130283
Email: mbordei@ugal.ro

AFFILIATED WITH:

- THE ROMANIAN SOCIETY FOR METALLURGY
- THE ROMANIAN SOCIETY FOR CHEMISTRY
- THE ROMANIAN SOCIETY FOR BIOMATERIALS
- THE ROMANIAN TECHNICAL FOUNDRY SOCIETY
- THE MATERIALS INFORMATION SOCIETY (ASM INTERNATIONAL)

Edited under the care of the FACULTY OF ENGINEERING

Annual subscription (4 issues per year)

Fascicle DOI: https://doi.org/10.35219/mms

Volume DOI: https://doi.org/10.35219/mms.2020.4

Editing date: 15.12.2020
Number of issues: 200
Printed by Galati University Press (accredited by CNCSIS)
47 Domneasca Street, 800008, Galati, Romania